Merging of storm-time midlatitude traveling ionospheric disturbances and equatorial plasma bubbles

Ercha Aa,[1,2] Shasha Zou,[2] Aaron Ridley,[2] Shunrong Zhang,[3] Anthea J. Coster,[3] Philip J. Erickson,[3] Siqing Liu,[1,4] and Jiaen Ren[2]

Correspondence to: E. Aa (aercha@nssc.ac.cn)

[1]National Space Science Center, Chinese Academy of Sciences, Beijing, China.

[2]Department of Climate and Space Sciences and Engineering, University of Michigan, Ann Arbor, MI, USA.

[3]Haystack Observatory, Massachusetts Institute of Technology, 99 Millstone Road, Westford, MA, USA.

[4]College of Earth and Planetary Science, University of Chinese Academy of Sciences, Beijing, China.

This is the author manuscript accepted for publication and has undergone full peer review but has not been through the copyediting, typesetting, pagination and proofreading process, which may lead to differences between this version and the Version of Record. Please cite this article as doi: 10.1029/2018SW002101

Abstract. Post-sunset midlatitude traveling ionospheric disturbances (TIDs) and equatorial plasma bubbles (EPBs) were simultaneously observed over American sector during the geomagnetic storm on 8 September 2017. The characteristics of TIDs are analyzed by using a combination of the Millstone Hill incoherent scatter radar (ISR) data and 2-D de-trended total electron content (TEC) from ground-based Global Navigation Satellite system (GNSS) receivers. The main results associated with EPBs are as follows: (1) stream-like structures of TEC depletion occurred simultaneously at geomagnetically conjugate points, (2) poleward extension of the TEC irregularities/depletions along the magnetic field lines, (3) severe equatorial and midlatitude electron density (Ne) bite-outs observed by DMSP and Swarm satellites, and (4) enhancements of ionosphere F-layer virtual height and vertical drifts observed by equatorial ionosondes near the EPBs initiation region. The stream-like TEC depletions reached 46° magnetic latitudes (MLAT) that map to an apex altitude of 6,800 km over the magnetic equator using IGRF. The formation of this extended density depletion structure is suggested to be due to the merging between the altitudinal/latitudinal extension of EPBs driven by strong prompt penetration electric field (PPEF) and midlatitude TIDs. Moreover, the poleward portion of the depletion/irregularity drifted westward and reached the equatorward boundary of the ionospheric main trough. This westward drift occurred at the same time as the sudden expansion of the convection pattern and could be attributed to the strong returning westward flow near

the subauroral polarization stream (SAPS) region. Other possible mechanisms for the westward tilt are also discussed.

1. Introduction

Geomagnetic storm can deposit considerable energy and momentum into auroral zone via precipitating particles, Joule heating, or Lorenz forces. These energy deposition can generate large amplitude atmospheric gravity waves (AGWs) that are manifested in the ionosphere as large-scale traveling ionospheric disturbances (LSTIDs) [*Hines*, 1960; *Hunsucker*, 1982]. LSTIDs normally have horizontal wavelengths of more than 1000 km, propagation speeds of 400–1000 m/s, and periods of 30–180 min. Besides LSTIDs, medium-scale TIDs (MSTIDs) are typically measured at midlatitudes during both quiet and disturbed conditions, which have horizontal wavelengths of several hundred kilometers, propagation speeds of 100–250 m/s, and periods of 15–60 min. For many years, TIDs have been intensively observed and studied by using different techniques, such as ionosondes [*Bowman*, 1992; *Afraimovich et al.*, 2008; *Bowman and Mortimer*, 2011], Doppler measurements of HF radars [*Jacobson and Carlos*, 1989; *Hayashi et al.*, 2010], incoherent scatter radars (ISR) [*Kirchengast et al.*, 1996; *Nicolls et al.*, 2004; *Nicolls and Heinselman*, 2007; *van de Kamp et al.*, 2014], and all-sky airglow imagers [*Shiokawa et al.*, 2003, 2005]. Recently, with the rapid growing of worldwide Global Navigation Satellite Systems (GNSS) receivers, the structure and evolution of TID have been further studied by using high-resolution ionospheric total electron content (TEC) maps [e.g. *Shiokawa et al.*, 2002; *Tsugawa et al.*, 2003, 2006; *Ding et al.*, 2007, 2008; *Otsuka et al.*, 2013; *Ding et al.*, 2014; *Pradipta et al.*, 2016; *Zakharenkova et al.*, 2016, etc.]. LSTIDs excited from the auroral zones can propagate toward the equator and experience various changes due to interaction with background ionosphere, such as energy dissipation caused by ion drag

[*Tsugawa et al.*, 2004] and changes in propagation velocity/period under the influence of thermospheric winds [*Ding et al.*, 2003]. Thus, the mid-to-low latitude ionosphere during storm time can be subjected to intrusions of TID perturbations originated from auroral latitudes.

On the other hand, the equatorial ionospheric irregular structures, such as equatorial plasma bubbles (EPBs), can be intensified and exhibit poleward expansion during a storm. Plasma bubbles appear mainly after sunset under the driving mechanism of the Rayleigh-Taylor (R-T) instability in the bottom-side ionosphere. The pre-reversal enhancement (PRE) of the zonal electric field can enhance the upward drift of the F-layer, which can increase the growth rate of R-T instability and thereby facilitate the development of EPBs [*Abdu*, 2005; *Huba and Joyce*, 2007; *Li et al.*, 2008; *Abadi et al.*, 2015; *Kil*, 2015]. During storm time, the occurrence of EPBs can be enhanced or suppressed due to two different perturbation electric fields: (1) the prompt penetration electric field (PPEF), which is created by solar wind-magnetosphere coupling after the southward turning of interplanetary magnetic field (IMF) B_z, can superpose upon the normal PRE to facilitate the development of EPBs on the duskside [*Abdu et al.*, 2003; *Basu et al.*, 2001, 2007; *Tulasi Ram et al.*, 2008; *Huang et al.*, 2010]; (2) ionospheric disturbance dynamo electric field (DDEF), which is caused by changes in global thermosphere circulation due to Joule heating in the auroral zone, can inhibit the occurrence of EPBs on the duskside [*Scherliess and Fejer*, 1997; *Li et al.*, 2009a; *Ramsingh et al.*, 2015; *Carter et al.*, 2016]. In addition, the substorm-related shielding electric field could also influence the zonal electric field [*Ebihara and Tanaka*, 2015; *Jin et al.*, 2018]. Moreover, several studies have found that under favorable storm-time PPEF/PRE conditions, the EPBs can rise to higher altitude with plasma depletion extending along the magnetic field lines to midlatitude regions [e.g. *Foster and Rich*, 1998; *Kelley et al.*, 2003; *Mendillo et al.*, 2005; *Ma and Maruyama*, 2006]; while in some extreme cases, the depletion signatures can even be measured around 40° magnetic latitude (MLAT) [e.g. *Martinis et al.*, 2005; *Cherniak and Zakharenkova*, 2016; *Katamzi-Joseph et al.*, 2017; *Aa et al.*, 2018]. Hence, the storm-time morphology of midlatitude ionosphere can be influenced by disturbances initiated from both auroral and equatorial regions.

Although there have been many observations of EPBs and TIDs, these two phenomena are usually studied separately. Actually these two processes can interact with each other to generate more complicated structures. Some studies have indicated that the AGW/TIDs can play a role of seed perturbation in triggering plasma bubbles [e.g. *Li et al.*, 2009b; *Krall et al.*, 2011; *Abdu et al.*, 2015; *Taori et al.*, 2015; *Li et al.*, 2016; *Takahashi et al.*, 2018]. Moreover, some other studies presented observations that the EPBs-related depletions can be embedded in or even counteracted by the wavy structures of TIDs [*Ogawa et al.*, 2005; *Ding et al.*, 2012; *Otsuka et al.*, 2012]. Considering the impact of these disturbances on space application systems as well as the above-mentioned scientific concerns, the coupling process of TIDs and EPBs is one of the key issues that worth further investigation. In this paper, we present a unique event with simultaneous observations of EPBs and TIDs over American sector during an intense storm on 8 September 2017. The evolutionary characteristics and coupling processes of these two phenomena are recorded and addressed by using measurements from ISR, dense GNSS network, Defense Meteorological Satellite Program (DMSP) and Swarm satellites, as well as ionosondes. It was found that the storm-time PPEF superposed on the normal PRE zonal electric field, which triggered the

EPBs with rapid upward plasma drift. The corresponding field-aligned extension of EPBs merged with midlatitude TIDs. The associated depletion structures extended to relatively high MLAT (46°), and then drifted westward reaching the equatorward boundary of the ionospheric main trough.

2. Data and Method

The most important ground-based measurements of EPBs and TIDs are TEC data derived from global and regional networks of GNSS receivers as are described in the acknowledgement section. The ionospheric TEC can be calculated by using the geometry-free linear combination of the pseudoranges and carrier phase measurements of GNSS receives with dual frequencies. For more details about the procedures of TEC derivation, readers may refer to *Aa et al.* [2015] and references therein. Overall data from more than 4000 GNSS receivers were processed. Moreover, the gridded TEC products from Madrigal database are also used here, which are developed at Massachusetts Institute of Technology (MIT) Haystack Observatory by using dense networks of worldwide GNSS receivers [*Rideout and Coster*, 2006; *Vierinen et al.*, 2016].

In order to extract the perturbation components in TEC data to represent the signatures of TID, the background trend of TEC is filtered out by using a method similar to those of *Shiokawa et al.* [2003], *Tsugawa et al.* [2007], and *Zakharenkova et al.* [2016]. A running average of TEC over 1 hour was subtracted from the raw data for all satellite-receiver paths. Then for each temporal-spatial grid of 1°×1°×10 min, the TEC perturbation is calculated by averaging all available de-trended vertical TEC values whose ionospheric pierce points (IPPs) crossed the grid. In this way, the two-dimensional de-trended TEC maps are constructed. Moreover, the EPBs-related ionospheric irregularities can be represented by using the two-dimensional maps of rate of TEC index (ROTI), which is defined as the 5-min standard deviation of the time derivative of TEC (Rate of TEC change, ROT) for all available satellite-receiver paths. Readers may refer to *Pi et al.* [1997] and *Cherniak et al.* [2014] to get more mathematical details on ROTI/ROT.

Besides TEC data, mid-latitude ionospheric information from the incoherent scatter radar at Millstone Hill (42.6°N, 288.5°E) as well as the in situ plasma density/drift measurements on board DMSP F17 and Swarm A/C satellites are used here to analyze the characteristics of LSTIDs and EPBs. Moreover, the ionosonde measurements from Jicamarca (12°S, 283.2°E; dip lat: 0.2°S), Campo Grande (20.5°S, 305°E; dip lat: 13.9°S), Sao Luis (2.6°S, 315.8°E; dip lat: 4.9°S), and Eglin AFB (30.5°N, 273.5°E; dip lat: 40.9°N) are also used here to study bubble features.

3. Geomagnetic Conditions of 7-8 September 2017

The solar wind and interplanetary magnetic field (IMF) conditions during 7-8 September 2017 have been described in several recent papers [e.g. *Aa et al.*, 2018; *Jin et al.*, 2018; *Lei et al.*, 2018; *Li et al.*, 2018; *Shen et al.*, 2018], which are also shown here in Figure 1a–1d. It was a storm with a double main phase. Multiple Coronal Mass Ejections (CMEs) associated with the X9.3 solar flare on 6 September 2017, reached Earth at 23:04 UT on 7 September 2017. After the shock arrival, the IMF Bz reached a minimum value of -31.2 nT at 23:31 UT, and remained southward for more than 2 hours. The symmetric index (SYM-H), which is the high-resolution Dst index, dropped to a minimum value of -146 nT at 01:08 UT on 8 September 2017. There was another drastic southward turning of IMF Bz, which reached -17.4 nT at 11:55 UT on 08 September and remained negative for several hours. The SYM-H dropped to a second minimum value of −115 nT at 13:56 UT on 8 September. We here focus on observations obtained during the first main phase.

4. Results

During the first main phase of the storm, the North American sector is around local dusk. In order to have an estimation about the equatorial electric field, the Prompt Penetration Equatorial Electric Field Model (PPEFM; *Manoj and Maus*, 2012) is used to calculate the PPEF and PRE around local dusk at U.S. longitudes, which is shown in Figure 1e with the time of PRE being marked by an arrow. It can be clearly seen that the PRE is drastically enhanced from 0.38 mV/m (quiet) to 0.94 mV/m (quiet plus penetration). Thus the post-sunset ionosphere in this sector is highly uplifted, which created a favorable condition for the formation of plasma bubbles. The TIDs features, on the other hand, can be observed from the ISR measurements at Millstone Hill observatory. It can be seen from the Ne and peak height results in Figure 1f that at least three oscillations of the F layer were recorded after the storm commencement with the second one raised the F peak to around 450 km. The vertical velocity data in Figure 1g also shows continuous fluctuations indicating wave-like structures of large-scale ionosphere activity with a period of around 1.5–2 hours, likely due to AGW initiated after the auroral energy deposition. In particular, large vertical drift (∼100 m/s) was observed after 01 UT on September 8 responsible for the F-region height increase to 450 km.

Figure 2 presents 4 snapshots of gridded TEC maps showing the evolution of EPBs over American sector on 7-8 September 2017. There was no signature of EPBs at 23:15 UT. After the drastic southward decreasing of IMF Bz at 23:31 UT, clear TEC depletion occurred over equatorial regions cutting through two EIA crests as can be seen in

Figure 2b, which represented the initiation of EPBs. Then the stream-like depletions gradually extended toward the Northern and Southern geomagnetically conjugate points at mid-to-high latitudes, forming an "inverted C-shape" as indicated by the arrows. The depth of the depletions varied in the range of 5–15 TEC Unit (TECU, 10^{16} el/m^2).

In order to further investigate these TEC depletions, in situ density measurements from multiple low Earth orbiting satellites are shown in Figure 3 and Figure 4. Figure 3a shows a global TEC map focusing on American sector at 01:00 UT on 08 September 2017, with the path of DMSP F17 satellite during 00:43–01:20 UT being superimposed. The azimuthally extended main trough can be clearly seen at the subauroral ionosphere in the form of TEC depletion. Besides the main trough, the "inverted C-shape" TEC depletion structures over midlatitude can also be observed. In the DMSP in situ plasma density/drift measurements shown in Figure 3b-3d, there were two depletion characteristics at midlatitude regions in the Northern (MLAT: 43°–47°N) and Southern (MLAT: 33°–38°S) Hemisphere, respectively. These plasma depletions were clearly separated from the subauroral polarization stream (SAPS; *Foster and Burke*, 2002) region that coincided with the ionospheric main trough, which are highlighted by the vertical dotted lines. The ion velocities of these midlatitude depletions are vertically downward, which are likely to be caused by the field-aligned component of the poleward plasma flow at this latitude. Through comparing Figure 3a and Figure 3b, it can be seen that the midlatitude plasma bite-outs in the DMSP Ne profile collocated well at the intersection of TEC depletion and satellite path. These midlatitude plasma depletions are the major focus of this study.

Figure 4a (Figure 4c) shows a TEC map focusing on the American sector at 03:00 UT (04:30 UT) with four consecutive orbits of Swarm A (Swarm C) satellite on 8 September

2017. The corresponding profiles of in situ electron density (Ne) along these orbits are shown as a function of geographic latitudes in Figure 4b and Figure 4d. The local magnetic equator is shown as a horizontal dotted line in each panel. Both Swarm A and Swarm C flew at an height of ∼450 km and were located at nearby longitudes around 10 LT (dayside) and 22 LT (nightside) between 60°N and 60°S. Swarm B satellite is not shown here because it did not pass through the American sector at local dusk hours in this period. Taking Swarm A as an example, the signature of EPBs can be clearly seen in orbit #1 (48.9°W), where a huge plasma depletion was located near the magnetic equator. Measured electron density was $4{\times}10^2$ el/cm^2, which was 2–3 orders of magnitude lower than the normal Ne profile. In orbit #2 (72.4°W) and #3 (95.8°W), there were still considerable plasma bite-outs over the magnetic equator, while one major branch of plasma depletion gradually propagated away from the equator toward the midlatitude regions, indicating the upward drift and the field-aligned extension of EPBs. Besides these bite-outs, the midlatitude trough can also be identified as a density decrease above ∼40° latitude in these plasma profiles. Similar results can also be found for Swarm C. The shaded areas indicate the sequential occurrence of plasma depletions over the equator, low latitudes, and midlatitude regions. These measurements are consistent with the poleward extension of TEC depletion and DMSP bite-outs structures in Figure 3.

Figure 5 shows a sequence of the de-trended TEC maps focusing on the American sector at 15-min intervals during 00:00–01:15 UT on 08 September 2017. The results clearly show the occurrence and propagation of TIDs with positive and negative phase fronts. Figure 5a indicates two distinct wave crests that appeared in the form of arc bands: the northern one stretched across Pacific-to-Atlantic coast over 40°N, which is co-located with the main trough; the southern one elongated aligned the Rocky mountains all the way to the Gulf of Mexico. During the next hour, these wavelike structures of TIDs propagated equatorward across North America with the estimated velocities of $\sim$300–400 m/s, wave amplitude of $\sim$0.8–1.0 TECU, wavelength of $\sim$1000–1200 km, and wave period of $\sim$50–60 min. The generation of these TIDs is expected due to the intensification of auroral activity and enhanced Joule heating after the strong southward turning during the storm. The shape of the wavefront of TIDs was mainly controlled by the wind pattern of thermosphere, the geomagnetic field, and the Coriolis effect [*Afraimovich et al.*, 2000]. Another thing worth noting is that in Figure 5a–5c, there were some tiny bifurcated structures of density decrease that occurred around 30°N near the duskside boundary of solar terminator, which look like nighttime midlatitude MSTIDs with west-tilted shape. Then started from 00:30 UT, those midlatitude branches merged with the poleward extension of low-latitude depletion structures, which elongated across two hemispheres.

In order to further verify the interaction of EPBs-related depletions and TIDs, Figure 6 shows the TEC ROTI maps over North America (10°–60°N, 60°–140°W) at 15-min intervals during 00:00-02:00 UT on 8 September 2017. A noticeable zone of irregularities can be seen over midlatitude trough/SAPS region. In addition, there was another obvious trace of irregularities, which was first seen around longitudinal sectors 70°–80°W in the low latitude regions at 00 UT (19 LT) and then propagated poleward. This propagating structure of irregularities corresponds to the upward drift and field-aligned extension of EPBs, which agrees well with the magnetic declination angle ($-10°$–$-15°$) in this longitudinal sector. At 00:30 UT, The trace of irregularities reached 40°N (MLAT: 46°N), which maps to an apex altitude of 6,800 km over the magnetic equator according to IGRF. After 00:30 UT, the irregularities stopped poleward migrating and started to drift westward reaching the equatorward boundary of the main trough. Thus, the results in Figure 5 and Figure 6 strengthened each other, which collectively illustrates the merging of EPBs-related depletions and the wavy structures of TIDs. Figure 7 shows similar ROTI results over South America. Also, the morphology of ROTI/TIDs variations agrees well with the satellites measurements in Figure 3 and Figure 4.

5. Discussion

First, there were noticeable plasma depletions over American sector in the local dusk on 8 September 2017 as can be seen from the results of TEC depletions, ROTI variations, and Ne bite-outs in the DMSP and Swarm satellites. Recall from Figure 1e, the sudden decreasing of IMF B_z right after the passage of solar terminator effectively triggered a drastic enhancement of PPEF, which penetrated nearly instantly into low latitude regions and maintained eastward for 1–2 hours before reverse. This strong PPEF is expected to lift the equatorial ionosphere to much higher altitudes, and created a quite favorable condition for EPBs to develop by increasing the growth rate of R-T instability. In order to further verify the PPEF and understand the development of EPBs, Figure 8 shows the corresponding variation of F-layer bottomside virtual height (h'F) over Jicamarca, as well as the vertical and zonal drift velocity components observed at Campo Grande and Sao Luis. These three ionosondes are located around geomagnetic equator. The zonal drift observed by ionosonde Eglin AFB at midlatitude region is also shown, which is located right at the depletion trace at 01 UT (Figure 3). The h'F over Jicamarca exhibited a significant post-sunset enhancements (marked with an arrow) that associated with the drastic decreasing of the IMF B_z. The vertical velocity drift over Campo Grande

(Figure 8c) and Sao Luis (Figure 8e) also displayed considerable increase compared with those on quiet day (6 September). Similar ionosonde measurements were also reported in *Li et al.* [2018], and these collectively demonstrate the presence of an enhanced equatorial PPEF to trigger EPBs.

Second, as EPBs-related depletions rise from the bottom-side ionosphere, they tend to form into wedge-like structures that extend along the magnetic field line. One prominent feature is that the depletions reached very high latitude in this case (MLAT: 46°N), which maps to an apex altitude of 6,800 km over the magnetic equator (L-shell ~2). Such deep depletion structures over midlatitude ranges have also been reported in a few studies [e.g. *Martinis et al.*, 2005; *Huang et al.*, 2007; *Cherniak and Zakharenkova*, 2016; *Aa et al.*, 2018; *Li et al.*, 2018]. One interpretation is that these midlatitude depletion structures are the field-aligned extension of EPBs that have risen to high apex heights, since these depletions can be detected at geomagnetically conjugate points in each hemisphere as was shown in Figure 2, which is similar with those pointed out in earlier studies [e.g. *Otsuka et al.*, 2002; *Shiokawa et al.*, 2004; *Martinis and Mendillo*, 2007; *Mendillo et al.*, 2018]. Besides strong PPEF, other processes have also been proposed to be able to assist in triggering of such depletion structures. A number of recent papers have discussed that large-scale wave structures in TIDs and/or coupling between local Perkins and sporadic E (Es) instabilities can play a role as seeding factors to trigger plasma irregularities [e.g. *Abdu et al.*, 2015; *Taori et al.*, 2015; *Li et al.*, 2016; *Takahashi et al.*, 2018]. Considering that the de-trended TEC maps also exhibit MSTID-like structures, the possibility that MSTIDs also played a role in the formation of the midlatitude depletions cannot be ruled out. Moreover, the observed depletions extended poleward and reached the equatorward boundary of the midlatitude trough/SAPS region, which is associated with the plasmasphere boundary layer [*Carpenter and Lemaire*, 2004; *Moldwin and Zou*, 2013]. Therefore, this density depletion might also be observed by equatorial orbiting satellite at low L shells. Previously, there have been reports about embedded low-density structures within the plasmasphere [*Horwitz et al.*, 1990; *Ober et al.*, 1997; *Huang et al.*, 2007]. *Fu et al.* [2010] reported that the low-density trough can be observed to extend from the plasmasphere to the topside ionosphere along the geomagnetic field lines. Whether this is related with the density depletions reported in current case is not clear, and conjugate observations will be needed in order to solve this problem.

Third, after 00:30 UT on 8 September 2017, the poleward extension of plasma depletion exhibited westward propagation and mixed with the wavy structures of TIDs as indicated both in Figure 5 and Figure 6. This west-tilted irregularity structure was also reported in the Asian sector during the second main phase for the same storm event [*Aa et al.*, 2018; *Li et al.*, 2018]. The thermospheric wind pattern has been suggested to be able to create such shape, which might be similar with those suggested by *Zhang et al.* [2015] and *Li et al.* [2018]. During geomagnetic quiet conditions, the zonal drift of plasma at the equatorial E-region is normally eastward due to solar-driven eastward wind; while at greater altitudes that map to higher latitudes, the density depletion structures tend to move slower than those at lower heights horizontally due to the decrease of eastward wind. In addition, *Kil et al.* [2009] and *Shiokawa et al.* [2015] also indicated that the polarization electric field developed inside the plasma depletion region could retard the eastward drift. These were suggested to be responsible for the west-tilted structure (so-called "inverted C-shape") in optical observations [e.g. *Otsuka et al.*, 2002; *Makela and Kelley*, 2003; *Kil et al.*, 2009;

Martinis et al., 2015]. However, during storm time, the eastward drift could be largely reduced or even reversed as can be seen from Figure 8d, 8f, and 8g that the storm-time zonal drift after local sunset was steadily westward. This westward reversal of EPBs drift has been reported in several studies with different triggering mechanisms being proposed, such as vertical Hall electric field induced by PPEF under enhanced E-layer conductivity [e.g. *Abdu et al.*, 2003; *Santos et al.*, 2016], and disturbance dynamo-associated westward thermospheric winds [e.g. *Sutton et al.*, 2005; *Abdu*, 2012; *Xiong et al.*, 2015]. In either scenario, the westward drift velocity is expected to increase from low to middle latitudes, which is in good agreement with ionosonde observations in current study.

In addition, the irregularity structures reached the equatorward boundary of the ionospheric main trough, where the westward convection flows can exist due to nighttime convection electric field penetrated into the plasmasphere or not completely shielded by the Region-2 system [*Lyons et al.*, 2009; *Zou et al.*, 2009]. In order to see whether westward convection flows may exist at the equatorward boundary of the trough, Figure 9 shows three consecutive polar plots of GNSS TEC maps over the Northern Hemisphere at 0050, 0100, and 0110 UT on 8 September 2017, which is superimposed with the ionospheric E×B convection pattern derived on the basis of Super Dual Auroral Radar Network (SuperDARN) measurements [*Ruohoniemi and Baker*, 1998; *Shepherd and Ruohoniemi*, 2000]. It can be seen based on the convection pattern and line-of-sight velocities that the main trough was co-located with very large convection return flows, i.e. SAPS. The bubble-related depletions gradually deepened near the equatorward boundary of the main trough at ∼20 MLT, which could be induced by these large convection flows near SAPS region through enhanced recombination in the ionosphere F-region height. Although the equatorward boundary of the returning flow cannot be fully revealed due to the limited field-of-view of the SuperDARN radar, the DMSP drift results in Figure 3 also indicates the existence of such large convection flows. Thus, the returning convection flow, the disturbance thermospheric wind, as well as the Hall electric field could collectively be responsible for the depletion/irregularity structures to drift westward along the wavefronts of LSTIDs. Considering the coupling process of TIDs and EPBs is still of rare study, more work, in particular numerical simulations, is needed in the future to further specify the dominant factor in triggering the EPB and the subsequent evolution.

6. Conclusion

This paper investigated the main characteristics and merging of postsunset EPBs and midlatitude TIDs over American sector during a storm on 8 September 2017. The spatial-temporal evolution and interaction of EPBs and TIDs can be simultaneously observed from the following measurements: (1) distinct stream-like structures of depletion (∼5–15 TECU) occurred at geomagnetically conjugate points in GNSS TEC maps, (2) severe plasma bite-outs of 2–3 orders at both equatorial and midlatitude regions in the Swarm/DMSP *Ne* profiles, (3) significant ROTI irregularities that propagated poleward along the field lines and then drifted westward, and (4) enhancements of ionosphere F-layer virtual height and vertical drifts observed at certain equatorial ionosondes. A prominent feature is that the plasma depletions reached very high latitudes (MLAT: 46°) that maps to an altitude of 6,800 km over the magnetic equator. The triggering mechanism of this mid-latitude depletion could be attributed to two possible mechanisms. One is that there were considerable altitudinal uplift and latitudinal extension of EPBs driven by strong eastward PPEF accompanied with drastic southward turning of IMF Bz in local dusk time, while TID wave structures might also play a role in forming these structures.

Moreover, there were intense LSTIDs that propagated equatorward in North America, as can be seen from the de-trended TEC maps and Ne/ion velocity fluctuations in the ISR results. One distinct feature is that the midlatitude depletion/irregularities drifted westward along the wavefronts of TIDs, forming into a longitudinally elongated structure that reached the equatorward boundary of the ionospheric main trough. This could be attributed to the large-scale convection returning flows equatorward of the SAPS region, while other mechanisms, such as the disturbance thermospheric westward wind could also make certain contribution. These processes collectively drove the midlatitude depletions to propagate westward, though more case studies and numerical modeling work are still needed in the future to specify the dominant mechanism.

Acknowledgments. This work is sponsored by the National Key R&D Program of China (2016YFB0501503), National Science Foundation of China (41404125, 41674183), AFOSR under DDDAS (Dynamic Data-Driven applications Systems http://www.1dddas.org/) grant FA9550-16-1-0071, and Youth Innovation Promotion Association of Chinese Academy of Sciences. The PPEFM results can be accessed from Cooperative Institute for Research in Environmental Sciences (http://geomag.org/models/PPEFM/RealtimeEF.html). We acknowledge ESA for SWARM data (http://earth.esa.int/swarm), NGDC NOAA for DMSP data (satdat.ngdc.noaa.gov/dmsp/), and NASA/GSFCs Space Physics Data Facilitys OMNIWeb service for geophysical parameters. We greatly appreciate the University of Massachusetts Lowell for providing ionosonde data from the DIDB database of Global Ionospheric Radio Observatory. GPS TEC data products, Millstone Hill incoherent scatter radar observations and analysis, and access through the Madrigal distributed data system are provided to the community (http://www.openmadrigal.org) by the Massachusetts Institute of Technology (MIT) under support from US National Science Foundation grant AGS-1242204. AJC, and SRZ acknowledge the ONR grant N00014-17-1-2186, and SRZ and AJC acknowledge the AFOSR MURI grant FA9559-16-1-0364. We also thank all participants in the worldwide SuperDARN collaboration for the distribution of SuperDARN data via: http://vt.superdarn.org/. We acknowledge the use of the raw GNSS data provided by IGS (ftp://cddis.gsfc.nasa.gov), the Scripps Orbit and Permanent Array Center (SOPAC; ftp://garner.ucsd.edu), the Continuously Operating Reference System (CORS; ftp://geodesy.noaa.gov), the EUREF Permanent GNSS network (EPN; ftp://olggps.oeaw.ac.at), the University NAVSTAR Consortium (UNAAVCO; ftp://data-out.unavco.org), Institut Geographique National in France (IGN; ftp://rgpdata.ign.fr), and the Brazilian Network for Continuous Monitoring (RBMC; ftp://geoftp.ibge.gov.br/RBMC/). Data for the TEC processing is also provided from the following organizations: National Geodetic Survey, Instituto Brasileiro de Geografia e Estatística, RAMSAC CORS of Instituto Geográfico Nacional de la República Argentina, Arecibo Observatory, Low-Latitude Ionospheric Sensor Network (LISN), Topcon Positioning Systems, Inc., Canadian High Arctic Ionospheric Network, Institute of Geology and Geophysics, Chinese Academy of Sciences, China Meteorology Administration, Centro di Ricerche Sismologiche, Système d'Observation du Niveau des Eaux Littorales (SONEL), RENAG : REseau NAtional GPS permanent, GeoNet - the official source of geological hazard information for New Zealand, GNSS Reference Networks, Finnish Meteorological Institute, and SWEPOS - Sweden.

References

Aa, E., W. Huang, S. Yu, S. Liu, L. Shi, J. Gong, Y. Chen, and H. Shen (2015), A regional ionospheric TEC mapping technique over China and adjacent areas on the basis of data assimilation, *J. Geophys. Res. Space Physics*, *120*, 5049–5061, doi: 10.1002/2015JA021140.

Aa, E., W. Huang, S. Liu, A. Ridley, S. Zou, L. Shi, Y. Chen, H. Shen, T. Yuan, J. Li, and T. Wang (2018), Midlatitude Plasma Bubbles Over China and Adjacent Areas During a Magnetic Storm on 8 September 2017, *Space Weather*, *16*, 321–331, doi:10.1002/2017SW001776.

Abadi, P., Y. Otsuka, and T. Tsugawa (2015), Effects of pre-reversal enhancement of E × B drift on the latitudinal extension of plasma bubble in Southeast Asia, *Earth Planets Space*, *67*, 74, doi:10.1186/s40623-015-0246-7.

Abdu, M. A. (2005), Equatorial ionosphere thermosphere system: Electrodynamics and irregularities, *Adv. Space Res.*, *35*, 771–787, doi:10.1016/j.asr.2005.03.150.

Abdu, M. A. (2012), Equatorial spread F/plasma bubble irregularities under storm time disturbance electric fields, *J. Atmos. Terr. Phys.*, *75*, 44–56, doi: 10.1016/j.jastp.2011.04.024.

Abdu, M. A., I. S. Batista, H. Takahashi, J. MacDougall, J. H. Sobral, A. F. Medeiros, and N. B. Trivedi (2003), Magnetospheric disturbance induced equatorial plasma bubble development and dynamics: A case study in Brazilian sector, *J. Geophys. Res.*, *108*, 1449, doi:10.1029/2002JA009721.

Abdu, M. A., J. R. Souza, E. A. Kherani, I. S. Batista, J. W. MacDougall, and J. H. A. Sobral (2015), Wave structure and polarization electric field development in the bottomside F layer leading to postsunset equatorial spread F, *J. Geophys. Res. Space Physics*, *120*, 6930–6940, doi:10.1002/2015JA021235.

Afraimovich, E. L., E. A. Kosogorov, L. A. Leonovich, K. S. Palamartchouk, N. P. Perevalova, and O. M. Pirog (2000), Observation of large-scale traveling ionospheric disturbances of auroral origin by global GPS networks, *Earth, Planets, and Space*, *52*, 669–674, doi:10.1186/BF03352261.

Afraimovich, E. L., S. V. Voeykov, N. P. Perevalova, and K. G. Ratovsky (2008), Large-scale traveling ionospheric disturbances of auroral origin according to the data of the GPS network and ionosondes, *Adv. Space Res.*, *42*, 1213–1217, doi:10.1016/j.asr.2007.11.023.

Basu, S., S. Basu, K. M. Groves, H.-C. Yeh, S.-Y. Su, F. J. Rich, P. J. Sultan, and M. J. Keskinen (2001), Response of the equatorial ionosphere in the South Atlantic Region to the Great Magnetic Storm of July 15, 2000, *Geophys. Res. Lett.*, *28*, 3577–3580, doi:10.1029/2001GL013259.

Basu, S., S. Basu, F. J. Rich, K. M. Groves, E. MacKenzie, C. Coker, Y. Sahai, P. R. Fagundes, and F. Becker-Guedes (2007), Response of the equatorial ionosphere at dusk to penetration electric fields during intense magnetic storms, *J. Geophys. Res.*, *112*, A08308, doi:10.1029/2006JA012192.

Bowman, G. G. (1992), Some aspects of large-scale travelling ionospheric disturbances, *Planet. Space Sci.*, *40*, 829–845, doi:10.1016/0032-0633(92)90110-A.

Bowman, G. G., and I. K. Mortimer (2011), Some aspects of large-scale travelling ionospheric disturbances which originate at conjugate locations in auroral zones, cross the equator and sometimes encircle the earth, *Ann. Geophys.*, *29*, 2203–2210, doi: 10.5194/angeo-29-2203-2011.

Carpenter, D., and J. Lemaire (2004), The Plasmasphere Boundary Layer, *Ann. Geophys.*, *22*, 4291–4298, doi:10.5194/angeo-22-4291-2004.

Carter, B. A., E. Yizengaw, R. Pradipta, J. M. Retterer, K. Groves, C. Valladares, R. Caton, C. Bridgwood, R. Norman, and K. Zhang (2016), Global equatorial plasma bubble occurrence during the 2015 St. Patrick's Day storm, *J. Geophys. Res. Space Physics*, *121*, 894–905, doi:10.1002/2015JA022194.

Cherniak, I., and I. Zakharenkova (2016), First observations of super plasma bubbles in Europe, *Geophys. Res. Lett.*, *43*, 11, doi:10.1002/2016GL071421.

Cherniak, I., A. Krankowski, and I. Zakharenkova (2014), Observation of the ionospheric irregularities over the Northern Hemisphere: Methodology and service, *Radio Sci.*, *49*, 653–662, doi:10.1002/2014RS005433.

Ding, F., W. Wan, and H. Yuan (2003), The influence of background winds and attenuation on the propagation of atmospheric gravity waves, *J. Atmos. Sol. Terr. Phys.*, *65*, 857–869, doi:10.1016/S1364-6826(03)00090-7.

Ding, F., W. Wan, B. Ning, and M. Wang (2007), Large-scale traveling ionospheric disturbances observed by GPS total electron content during the magnetic storm of 29-30 October 2003, *J. Geophys. Res.*, *112*, A06309, doi:10.1029/2006JA012013.

Ding, F., W. Wan, L. Liu, E. L. Afraimovich, S. V. Voeykov, and N. P. Perevalova (2008), A statistical study of large-scale traveling ionospheric disturbances observed by GPS

TEC during major magnetic storms over the years 2003-2005, *J. Geophys. Res.*, *113*, A00A01, doi:10.1029/2008JA013037.

Ding, F., W. Wan, B. Ning, B. Zhao, Q. Li, R. Zhang, B. Xiong, and Q. Song (2012), Two-dimensional imaging of large-scale traveling ionospheric disturbances over China based on GPS data, *J. Geophys. Res.*, *117*, A08318, doi:10.1029/2012JA017546.

Ding, F., W. Wan, Q. Li, R. Zhang, Q. Song, B. Ning, L. Liu, B. Zhao, and B. Xiong (2014), Comparative climatological study of large-scale traveling ionospheric disturbances over North America and China in 2011-2012, *J. Geophys. Res. Space Physics*, *119*, 519–529, doi:10.1002/2013JA019523.

Ebihara, Y., and T. Tanaka (2015), Substorm simulation: Insight into the mechanisms of initial brightening, *J. Geophys. Res. Space Physics*, *120*, 7270–7288, doi:10.1002/2015JA021516.

Foster, J. C., and W. J. Burke (2002), SAPS: A new categorization for sub-auroral electric fields, *EOS Trans.*, *83*, 393, doi:10.1029/2002EO000289.

Foster, J. C., and F. J. Rich (1998), Prompt midlatitude electric field effects during severe geomagnetic storms, *J. Geophys. Res.*, *103*, 26,367–26,372, doi:10.1029/97JA03057.

Fu, H. S., J. Tu, J. B. Cao, P. Song, B. W. Reinisch, D. L. Gallagher, and B. Yang (2010), IMAGE and DMSP observations of a density trough inside the plasmasphere, *J. Geophys. Res.*, *115*, A07227, doi:10.1029/2009JA015104.

Hayashi, H., N. Nishitani, T. Ogawa, Y. Otsuka, T. Tsugawa, K. Hosokawa, and A. Saito (2010), Large-scale traveling ionospheric disturbance observed by superDARN Hokkaido HF radar and GPS networks on 15 December 2006, *J. Geophys. Res.*, *115*, A06309, doi:10.1029/2009JA014297.

Hines, C. O. (1960), Internal atmospheric gravity waves at ionospheric heights, *Can. J. Phys.*, *38*, 1441, doi:10.1139/p60-150.

Horwitz, J. L., R. H. Comfort, and C. R. Chappell (1990), A statistical characterization of plasmasphere density structure and boundary locations, *J. Geophys. Res.*, *95*, 7937–7947, doi:10.1029/JA095iA06p07937.

Huang, C.-S., J. C. Foster, and Y. Sahai (2007), Significant depletions of the ionospheric plasma density at middle latitudes: A possible signature of equatorial spread F bubbles near the plasmapause, *J. Geophys. Res.*, *112*, A05315, doi:10.1029/2007JA012307.

Huang, C.-S., F. J. Rich, and W. J. Burke (2010), Storm time electric fields in the equatorial ionosphere observed near the dusk meridian, *J. Geophys. Res.*, *115*, A08313, doi:10.1029/2009JA015150.

Huba, J. D., and G. Joyce (2007), Equatorial spread F modeling: Multiple bifurcated structures, secondary instabilities, large density 'bite-outs,' and supersonic flows, *Geophys. Res. Lett.*, *34*, L07105, doi:10.1029/2006GL028519.

Hunsucker, R. D. (1982), Atmospheric gravity waves generated in the high-latitude ionosphere: A review, *Rev. Geophys. Space Phys.*, *20*, 293–315, doi:10.1029/RG020i002p00293.

Jacobson, A. R., and R. C. Carlos (1989), Coherent-array HF Doppler sounding of traveling ionospheric disturbances. I - Basic technique, *J. Atmos. Terr. Phys.*, *51*, 297–309, doi:10.1016/0021-9169(89)90081-0.

Jin, H., S. Zou, G. Chen, C. Yan, and G. Zhang, S. andbYang (2018), Formation and Evolution of Low-Latitude F Region Field-Aligned Irregularities During the 7-8 September 2017 Storm: Hainan Coherent Scatter Phased Array Radar and Digisonde Observations, *Space Weather*, *16*, 648–659, doi:10.1029/2018SW001865.

Katamzi-Joseph, Z. T., J. B. Habarulema, and M. Hernández-Pajares (2017), Midlatitude postsunset plasma bubbles observed over europe during intense storms in april 2000 and 2001, *Space Weather*, *15*(9), 1177–1190, doi:10.1002/2017SW001674.

Kelley, M. C., J. J. Makela, L. J. Paxton, F. Kamalabadi, J. M. Comberiate, and H. Kil (2003), The first coordinated ground- and space-based optical observations of equatorial plasma bubbles, *Geophys. Res. Lett.*, *30*, 1766, doi:10.1029/2003GL017301.

Kil, H. (2015), The Morphology of Equatorial Plasma Bubbles - a review, *J. Astron. Space Sci.*, *32*, 13–19, doi:10.5140/JASS.2015.32.1.13.

Kil, H., R. A. Heelis, L. J. Paxton, and S.-J. Oh (2009), Formation of a plasma depletion shell in the equatorial ionosphere, *J. Geophys. Res.*, *114*, A11302, doi: 10.1029/2009JA014369.

Kirchengast, G., K. Hocke, and K. Schlegel (1996), The gravity wave - TID relationship: insight via theoretical model - EISCAT data comparison., *J. Atmos. Terr. Phys.*, *58*, 233–243, doi:10.1016/0021-9169(95)00032-1.

Krall, J., J. D. Huba, S. L. Ossakow, G. Joyce, J. J. Makela, E. S. Miller, and M. C. Kelley (2011), Modeling of equatorial plasma bubbles triggered by non-equatorial traveling ionospheric disturbances, *Geophys. Res. Lett.*, *38*, L08103, doi:10.1029/2011GL046890.

Lei, J., F. Huang, X. Chen, J. Zhong, D. Ren, W. Wang, X. Yue, X. Luan, M. Jia, X. Dou, L. Hu, B. Ning, C. Owolabi, J. Chen, G. Li, and X. Xue (2018), Was Magnetic Storm the Only Driver of the Long-Duration Enhancements of Daytime Total Electron Content in the Asian-Australian Sector Between 7 and 12 September 2017?, *J. Geophys. Res. Space Physics*, *123*, 3217–3232, doi:10.1029/2017JA025166.

Li, G., B. Ning, L. Liu, B. Zhao, X. Yue, S.-Y. Su, and S. Venkatraman (2008), Correlative study of plasma bubbles, evening equatorial ionization anomaly, and equatorial prereversal E × B drifts at solar maximum, *Radio Sci.*, *43*, RS4005, doi:10.1029/2007RS003760.

Li, G., B. Ning, L. Liu, W. Wan, and J. Y. Liu (2009a), Effect of magnetic activity on plasma bubbles over equatorial and low-latitude regions in East Asia, *Ann. Geophys.*, *27*, 303–312, doi:10.5194/angeo-27-303-2009.

Li, G., B. Ning, B. Zhao, L. Liu, W. Wan, F. Ding, J. S. Xu, J. Y. Liu, and K. Yumoto (2009b), Characterizing the 10 November 2004 storm-time middle-latitude plasma bubble event in Southeast Asia using multi-instrument observations, *J. Geophys. Res.*, *114*, A07304, doi:10.1029/2009JA014057.

Li, G., Y. Otsuka, B. Ning, M. A. Abdu, M. Yamamoto, W. Wan, L. Liu, and P. Abadi (2016), Enhanced ionospheric plasma bubble generation in more active ITCZ, *Geophys. Res. Lett.*, *43*, 2389–2395, doi:10.1002/2016GL068145.

Li, G., B. Ning, C. Wang, M. A. Abdu, Y. Otsuka, M. Yamamoto, J. Wu, and J. Chen (2018), Storm-enhanced development of post-sunset equatorial plasma bubbles around the meridian 120E/60W on 7-8 September 2017, *J. Geophys. Res. Space Physics*, *123*, 1–16, doi:10.1029/2018JA025871.

Lyons, L. R., S. Zou, C. J. Heinselman, M. J. Nicolls, and P. C. Anderson (2009), Poker flat radar observations of the magnetosphere-ionosphere coupling electrodynamics of the earthward penetrating plasma sheet following convection enhancements, *J. Atmos. Sol. Terr. Phys.*, *71*, 717–728, doi:10.1016/j.jastp.2008.09.025.

Ma, G., and T. Maruyama (2006), A super bubble detected by dense GPS network at east Asian longitudes, *Geophys. Res. Lett.*, *33*, L21103, doi:10.1029/2006GL027512.

Makela, J. J., and M. C. Kelley (2003), Field-aligned 777.4-nm composite airglow images of equatorial plasma depletions, *Geophys. Res. Lett.*, *30*, 1442, doi:10.1029/2003GL017106.

Manoj, C., and S. Maus (2012), A real-time forecast service for the ionospheric equatorial zonal electric field, *Space Weather*, *10*, S09002, doi:10.1029/2012SW000825.

Martinis, C., and M. Mendillo (2007), Equatorial spread F-related airglow depletions at Arecibo and conjugate observations, *J. Geophys. Res.*, *112*, A10310, doi: 10.1029/2007JA012403.

Martinis, C., J. Baumgardner, M. Mendillo, J. Wroten, A. Coster, and L. Paxton (2015), The night when the auroral and equatorial ionospheres converged, *J. Geophys. Res. Space Physics*, *120*, 8085–8095, doi:10.1002/2015JA021555.

Martinis, C. R., M. J. Mendillo, and J. Aarons (2005), Toward a synthesis of equatorial spread F onset and suppression during geomagnetic storms, *J. Geophys. Res.*, *110*, A07306, doi:10.1029/2003JA010362.

Mendillo, M., E. Zesta, S. Shodhan, P. J. Sultan, R. Doe, Y. Sahai, and J. Baumgardner (2005), Observations and modeling of the coupled latitude-altitude patterns of equatorial plasma depletions, *J. Geophys. Res.*, *110*, A09303, doi:10.1029/2005JA011157.

Mendillo, M., D. Hickey, C. Martinis, J. Wroten, and J. Baumgardner (2018), Space weather nowcasting for area-denied locations: Testing all-sky imaging applications at geomagnetic conjugate points, *Space Weather*, *16*(1), 47–56, doi:10.1002/2017SW001741.

Moldwin, M., and S. Zou (2013), *The Importance of the Plasmasphere Boundary Layer for Understanding Inner Magnetosphere Dynamics*, pp. 321–328, American Geophysical Union (AGU), doi:10.1029/2012GM001323.

Nicolls, M. J., and C. J. Heinselman (2007), Three-dimensional measurements of traveling ionospheric disturbances with the Poker Flat Incoherent Scatter Radar, *Geophys. Res. Lett.*, *34*, L21104, doi:10.1029/2007GL031506.

Nicolls, M. J., M. C. Kelley, A. J. Coster, S. A. González, and J. J. Makela (2004), Imaging the structure of a large-scale TID using ISR and TEC data, *Geophys. Res. Lett.*, *31*, L09812, doi:10.1029/2004GL019797.

Ober, D. M., J. L. Horwitz, and D. L. Gallagher (1997), Formation of density troughs embedded in the outer plasmasphere by subauroral ion drift events, *J. Geophys. Res.*, *102*, 14,595–14,602, doi:10.1029/97JA01046.

Ogawa, T., E. Sagawa, Y. Otsuka, K. Shiokawa, T. I. Immel, S. B. Mende, and P. Wilkinson (2005), Simultaneous ground- and satellite-based airglow observations of geomagnetic conjugate plasma bubbles in the equatorial anomaly, *Earth Planets Space*, *57*, 385–392, doi:10.1186/BF03351822.

Otsuka, Y., K. Shiokawa, T. Ogawa, and P. Wilkinson (2002), Geomagnetic conjugate observations of equatorial airglow depletions, *Geophys. Res. Lett.*, *29*, 1753, doi: 10.1029/2002GL015347.

Otsuka, Y., K. Shiokawa, and T. Ogawa (2012), Disappearance of equatorial plasma bubble after interaction with mid-latitude medium-scale traveling ionospheric disturbance, *Geophys. Res. Lett.*, *39*, L14105, doi:10.1029/2012GL052286.

Otsuka, Y., K. Suzuki, S. Nakagawa, M. Nishioka, K. Shiokawa, and T. Tsugawa (2013), GPS observations of medium-scale traveling ionospheric disturbances over Europe, *Ann. Geophys.*, *31*, 163–172, doi:10.5194/angeo-31-163-2013.

Pi, X., A. J. Mannucci, U. J. Lindqwister, and C. M. Ho (1997), Monitoring of global ionospheric irregularities using the Worldwide GPS Network, *Geophys. Res. Lett.*, *24*, 2283–2286, doi:10.1029/97GL02273.

Pradipta, R., C. E. Valladares, B. A. Carter, and P. H. Doherty (2016), Interhemispheric propagation and interactions of auroral traveling ionospheric disturbances near the equator, *J. Geophys. Res. Space Physics*, *121*, 2462–2474, doi:10.1002/2015JA022043.

Ramsingh, S. Sripathi, S. Sreekumar, S. Banola, K. Emperumal, P. Tiwari, and B. S. Kumar (2015), Low-latitude ionosphere response to super geomagnetic storm of 17/18 March 2015: Results from a chain of ground-based observations over Indian sector, *J. Geophys. Res. Space Physics*, *120*, 10, doi:10.1002/2015JA021509.

Rideout, W., and A. Coster (2006), Automated gps processing for global total electron content data, *GPS Solut.*, *10*(3), 219–228, doi:10.1007/s10291-006-0029-5.

Ruohoniemi, J. M., and K. B. Baker (1998), Large-scale imaging of high-latitude convection with Super Dual Auroral Radar Network HF radar observations, *J. Geophys. Res.*, *103*, 20,797–20,811, doi:10.1029/98JA01288.

Santos, A. M., M. A. Abdu, J. R. Souza, J. H. A. Sobral, I. S. Batista, and C. M. Denardini (2016), Storm time equatorial plasma bubble zonal drift reversal due to disturbance Hall electric field over the Brazilian region, *J. Geophys. Res. Space Physics*, *121*, 5594–5612, doi:10.1002/2015JA022179.

Scherliess, L., and B. G. Fejer (1997), Storm time dependence of equatorial disturbance dynamo zonal electric fields, *J. Geophys. Res.*, *102*, 24,037–24,046, doi:10.1029/97JA02165.

Shen, C., M. Xu, Y. Wang, Y. Chi, and B. Luo (2018), Why the Shock-ICME Complex Structure Is Important: Learning from the Early 2017 September CMEs, *Astrophysical Journal*, *861*, 28, doi:10.3847/1538-4357/aac204.

Shepherd, S. G., and J. M. Ruohoniemi (2000), Electrostatic potential patterns in the high-latitude ionosphere constrained by SuperDARN measurements, *J. Geophys. Res.*, *105*, 23,005–23,014, doi:10.1029/2000JA000171.

Shiokawa, K., Y. Otsuka, T. Ogawa, N. Balan, K. Igarashi, A. J. Ridley, D. J. Knipp, A. Saito, and K. Yumoto (2002), A large-scale traveling ionospheric disturbance during the magnetic storm of 15 September 1999, *J. Geophys. Res.*, *107*, 1088, doi:10.1029/2001JA000245.

Shiokawa, K., Y. Otsuka, T. Ogawa, S. Kawamura, M. Yamamoto, S. Fukao, T. Nakamura, T. Tsuda, N. Balan, K. Igarashi, G. Lu, A. Saito, and K. Yumoto (2003), Thermospheric wind during a storm-time large-scale traveling ionospheric disturbance, *J. Geophys. Res.*, *108*, 1423, doi:10.1029/2003JA010001.

Shiokawa, K., Y. Otsuka, T. Ogawa, and P. Wilkinson (2004), Time evolution of high-altitude plasma bubbles imaged at geomagnetic conjugate points, *Ann. Geophys.*, *22*, 3137–3143, doi:10.5194/angeo-22-3137-2004.

Shiokawa, K., Y. Otsuka, T. Tsugawa, T. Ogawa, A. Saito, K. Ohshima, M. Kubota, T. Maruyama, T. Nakamura, M. Yamamoto, and P. Wilkinson (2005), Geomagnetic conjugate observation of nighttime medium-scale and large-scale traveling ionospheric disturbances: FRONT3 campaign, *J. Geophys. Res.*, *110*, A05303, doi:10.1029/2004JA010845.

Shiokawa, K., Y. Otsuka, K. J. Lynn, P. Wilkinson, and T. Tsugawa (2015), Airglow-imaging observation of plasma bubble disappearance at geomagnetically conjugate points, *Earth Planets Space*, *67*, 43, doi:10.1186/s40623-015-0202-6.

Sutton, E. K., J. M. Forbes, and R. S. Nerem (2005), Global thermospheric neutral density and wind response to the severe 2003 geomagnetic storms from CHAMP accelerometer data, *J. Geophys. Res.*, *110*, A09S40, doi:10.1029/2004JA010985.

Takahashi, H., C. M. Wrasse, C. A. O. B. Figueiredo, D. Barros, M. A. Abdu, Y. Otsuka, and K. Shiokawa (2018), Equatorial plasma bubble seeding by MSTIDs in the ionosphere, *Progress in Earth and Planetary Science*, *5*, 32, doi:10.1186/s40645-018-0189-2.

Taori, A., N. Parihar, R. Ghodpage, N. Dashora, S. Sripathi, E. A. Kherani, and P. T. Patil (2015), Probing the possible trigger mechanisms of an equatorial plasma bubble event based on multistation optical data, *J. Geophys. Res. Space Physics*, *120*, 8835–8847, doi:10.1002/2015JA021541.

Tsugawa, T., A. Saito, Y. Otsuka, and M. Yamamoto (2003), Damping of large-scale traveling ionospheric disturbances detected with GPS networks during the geomagnetic storm, *J. Geophys. Res.*, *108*, 1127, doi:10.1029/2002JA009433.

Tsugawa, T., A. Saito, and Y. Otsuka (2004), A statistical study of large-scale traveling ionospheric disturbances using the GPS network in Japan, *J. Geophys. Res.*, *109*, A06302, doi:10.1029/2003JA010302.

Tsugawa, T., K. Shiokawa, Y. Otsuka, T. Ogawa, A. Saito, and M. Nishioka (2006), Geomagnetic conjugate observations of large-scale traveling ionospheric disturbances using GPS networks in Japan and Australia, *J. Geophys. Res.*, *111*, A02302, doi:10.1029/2005JA011300.

Tsugawa, T., Y. Otsuka, A. J. Coster, and A. Saito (2007), Medium-scale traveling ionospheric disturbances detected with dense and wide TEC maps over North America, *Geophys. Res. Lett.*, *34*, L22101, doi:10.1029/2007GL031663.

Tulasi Ram, S., P. V. S. Rama Rao, D. S. V. V. D. Prasad, K. Niranjan, S. Gopi

Krishna, R. Sridharan, and S. Ravindran (2008), Local time dependent response of postsunset ESF during geomagnetic storms, *J. Geophys. Res.*, *113*, A07310, doi: 10.1029/2007JA012922.

van de Kamp, M., D. Pokhotelov, and K. Kauristie (2014), TID characterised using joint effort of incoherent scatter radar and GPS, *Ann. Geophys.*, *32*, 1511–1532, doi: 10.5194/angeo-32-1511-2014.

Vierinen, J., A. J. Coster, W. C. Rideout, P. J. Erickson, and J. Norberg (2016), Statistical framework for estimating GNSS bias, *Atmospheric Measurement Techniques*, *9*, 1303–1312, doi:10.5194/amt-9-1303-2016.

Xiong, C., H. Lühr, and B. G. Fejer (2015), Global features of the disturbance winds during storm time deduced from CHAMP observations, *J. Geophys. Res. Space Physics*, *120*, 5137–5150, doi:10.1002/2015JA021302.

Zakharenkova, I., E. Astafyeva, and I. Cherniak (2016), GPS and GLONASS observations of large-scale traveling ionospheric disturbances during the 2015 St. Patrick's Day storm, *J. Geophys. Res. Space Physics*, *121*, 12, doi:10.1002/2016JA023332.

Zhang, S.-R., P. J. Erickson, J. C. Foster, J. M. Holt, A. J. Coster, J. J. Makela, J. Noto, J. W. Meriwether, B. J. Harding, J. Riccobono, and R. B. Kerr (2015), Thermospheric poleward wind surge at midlatitudes during great storm intervals, *Geophys. Res. Lett.*, *42*, 5132–5140, doi:10.1002/2015GL064836.

Zou, S., L. R. Lyons, M. J. Nicolls, C. J. Heinselman, and S. B. Mende (2009), Night-side ionospheric electrodynamics associated with substorms: PFISR and THEMIS ASI observations, *J. Geophys. Res.*, *114*, A12301, doi:10.1029/2009JA014259.

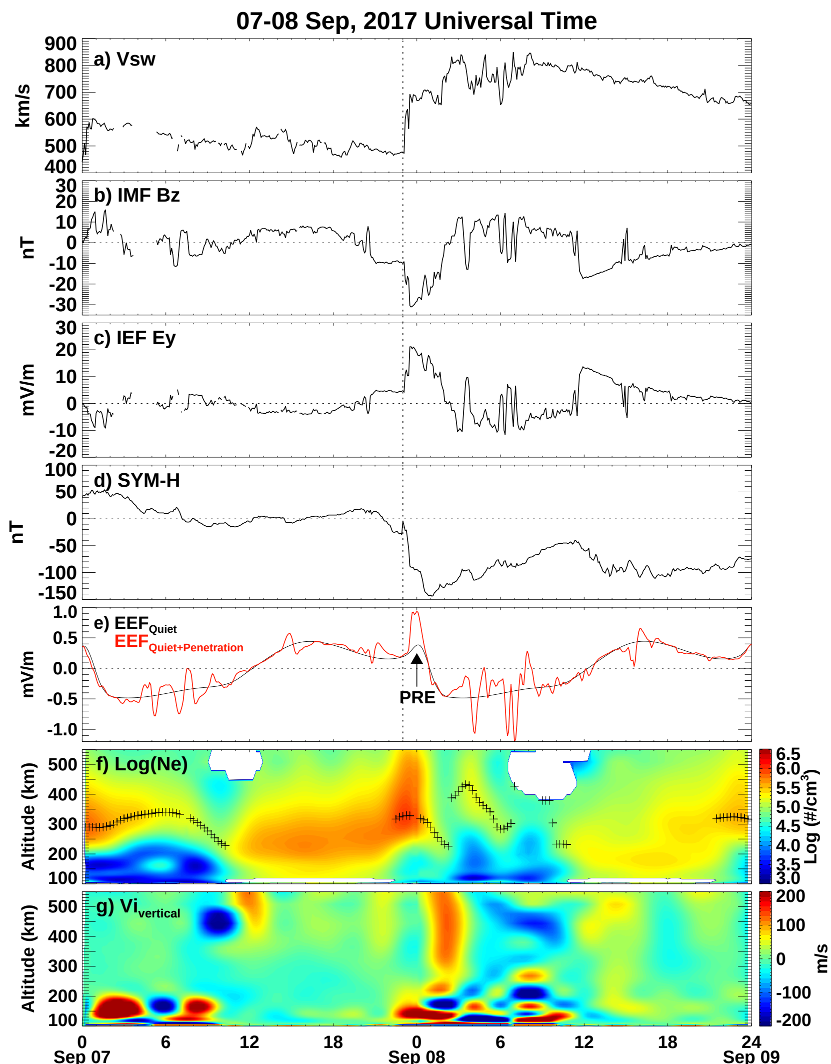

Figure 1. Parameters variation during the period of 7-8 September 2017: (a) Solar wind speed, (b) interplanetary magnetic field (IMF) B_z, (c) interplanetary electric field (IEF) E_y, (d) SYM-H index, (e) equatorial electrical field (EEF) at 80°W for quiet time (black) and quiet plus penetration (red), (f) Log electron density profile marked with peak height (asterisk), and (g) vertical ion velocity profile. The solar wind and IMF data have been shifted to the nose of the Earth's bow shock. The vertical dotted line represent the storm sudden commencement (SSC).

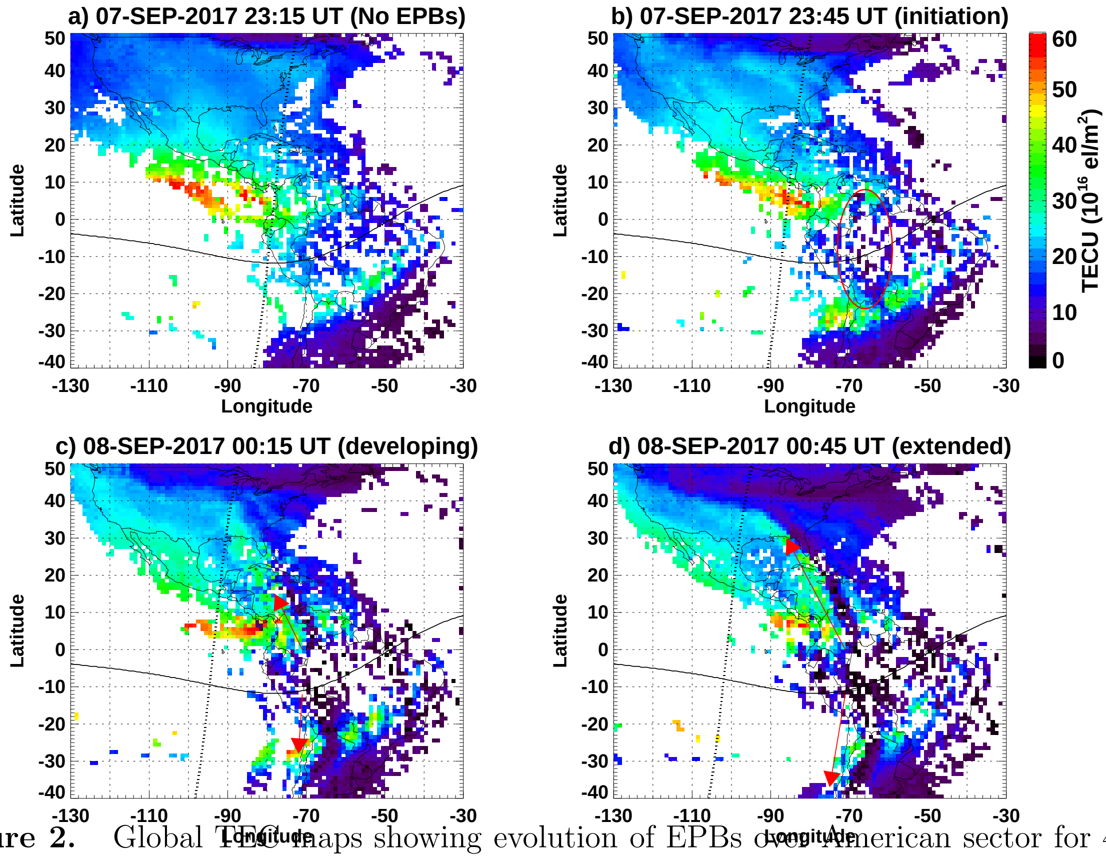

Figure 2. Global TEC maps showing evolution of EPBs over American sector for 4 different time instants on 7-8 September 2017. The terminator and magnetic equator are marked with dotted and solid lines, respectively.

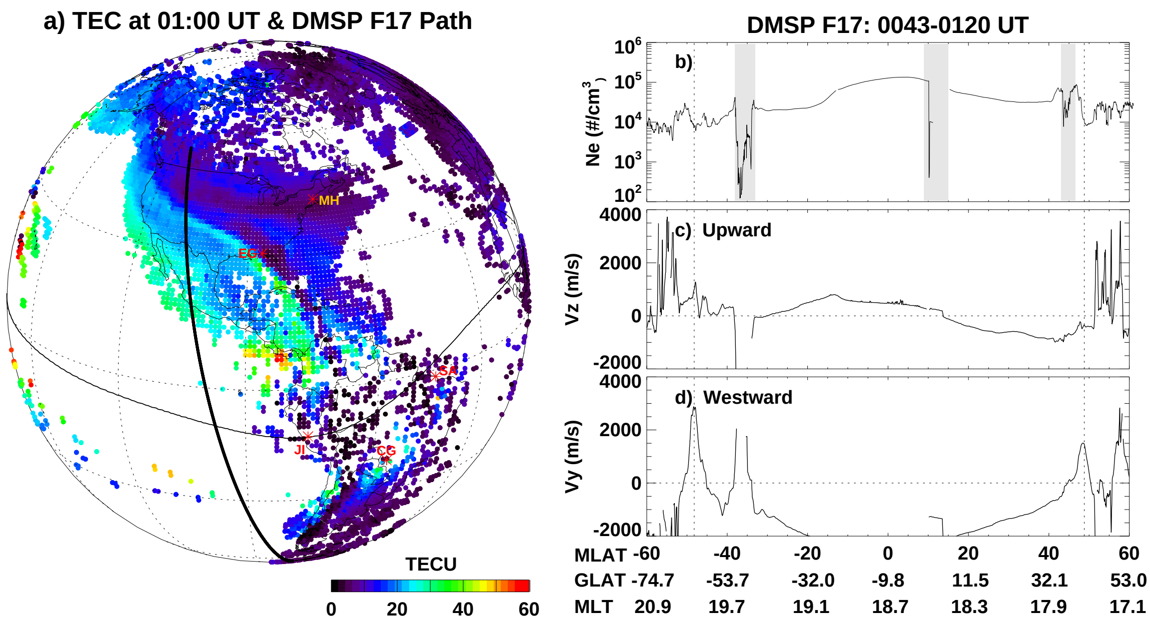

Figure 3. (a) Global TEC map at 01:00 UT on 8 September 2017, with path of DMSP F17 satellite and geomagnetic equator being superimposed. Latitudinal distribution of the (b) ionospheric ion density, (c) vertical velocity component, and (d) horizontal velocity component. Five different asterisks mark the location of Millstone Hill (MH), Eglin AFB (EG), Jicamarca (JI), Campo Grande (CG), and Sao Luis (SA), respectively. The shaded areas represent deep plasma depletions. The vertical dotted lines indicate the location of the ion horizontal velocity peak in the SAPS region and the midlatitude troughs.

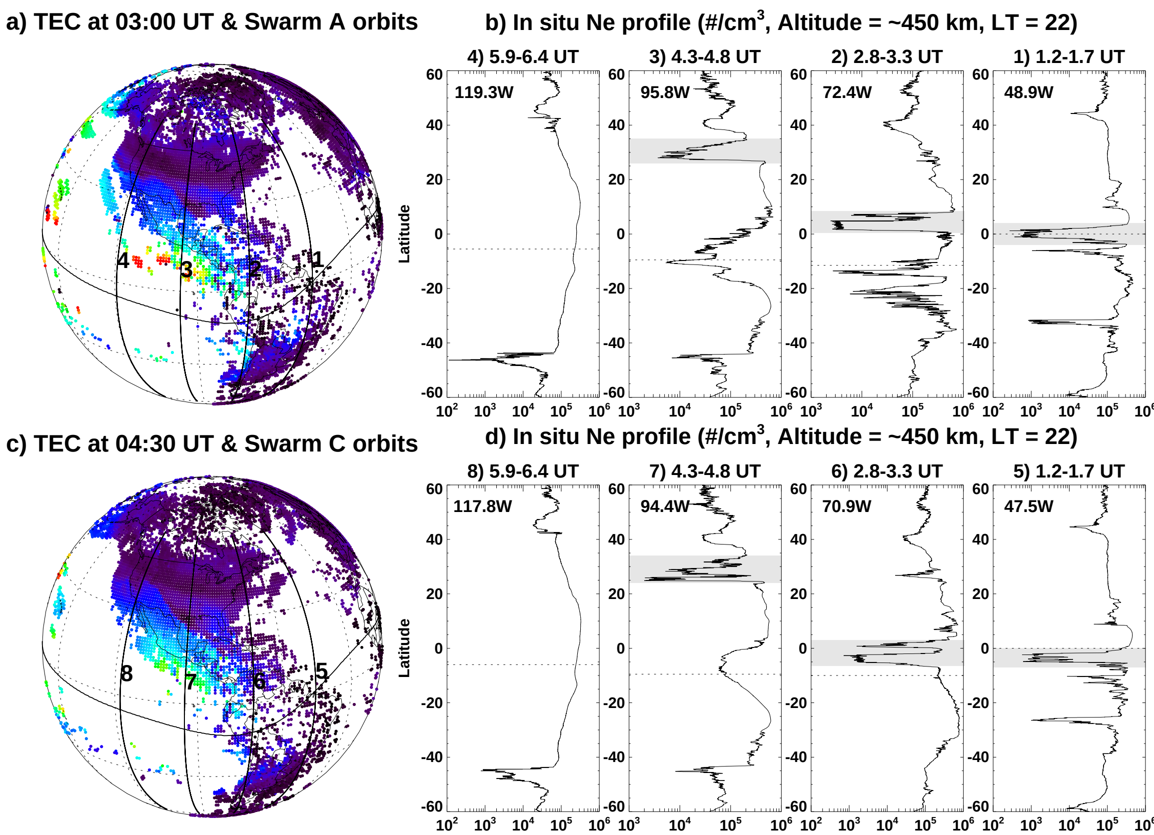

Figure 4. (a) The global TEC map focusing on American sector at 03:00 UT with 4 consecutive satellite paths of Swarm A. (b) Variation of in situ electron density as a function of geographic latitudes along these paths. (c) and (d): The same as Figure 3a and Figure 3b respectively, but for TEC map at 04:30 UT and Swarm C satellite. The magnetic equator is marked by solid line in left panels and dotted line in right panels.

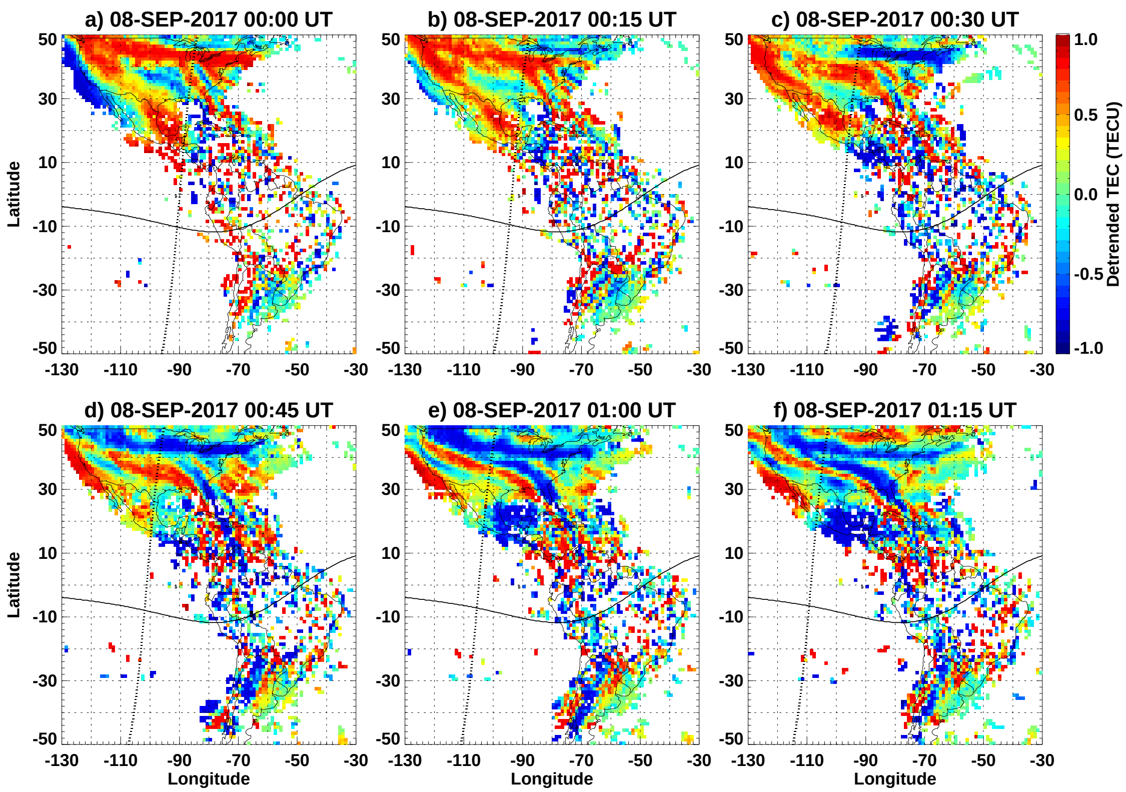

Figure 5. De-trended TEC maps focusing on American sector for different time instants on 8 September 2017. The terminator and magnetic equator are marked with dotted and solid lines, respectively.

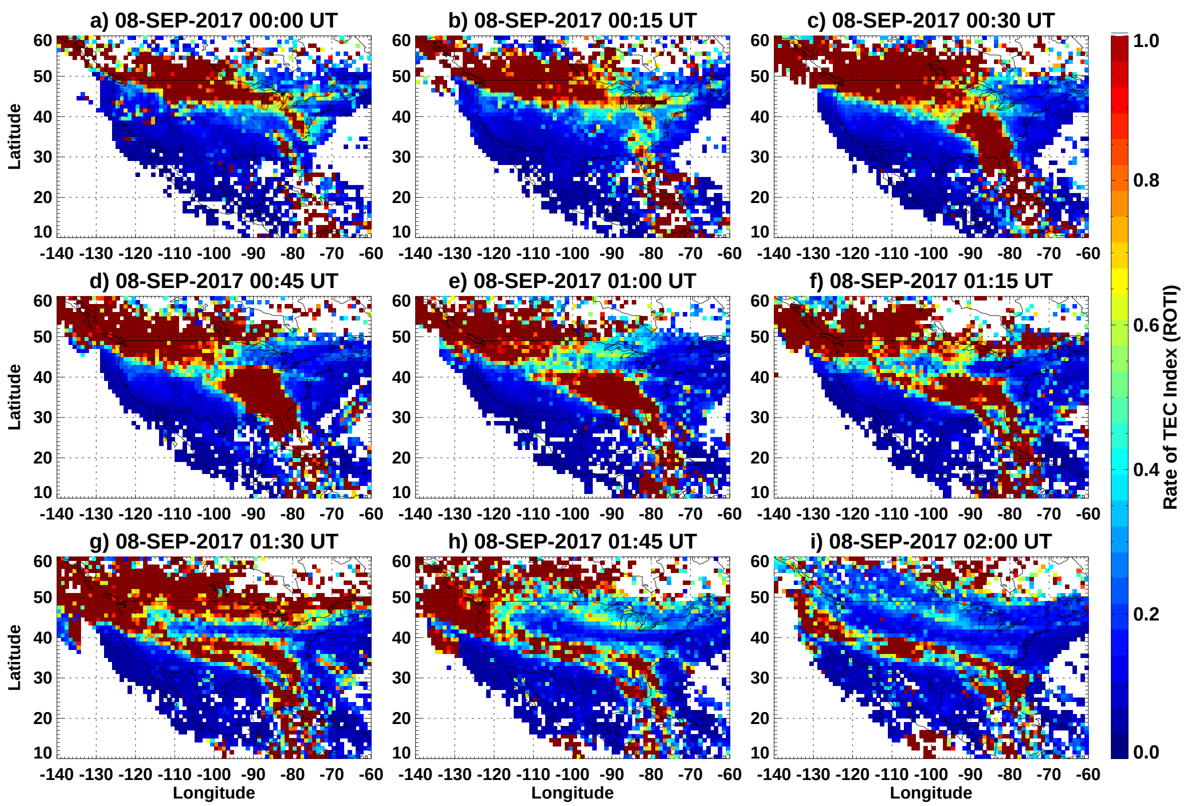

Figure 6. ROTI maps of ionospheric irregularities over North American regions with 15 min interval during 00:00-02:00 UT on 8 September 2017.

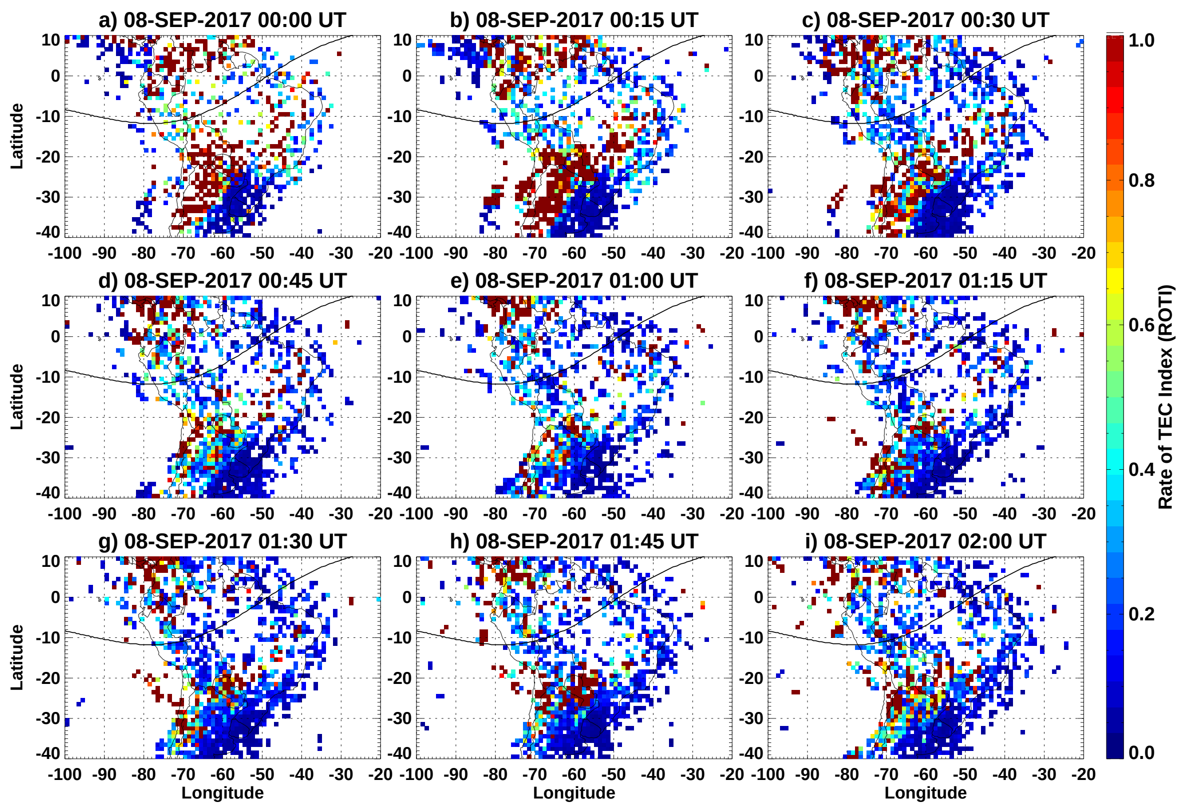

Figure 7. The same as Figure 6, but for South American regions.

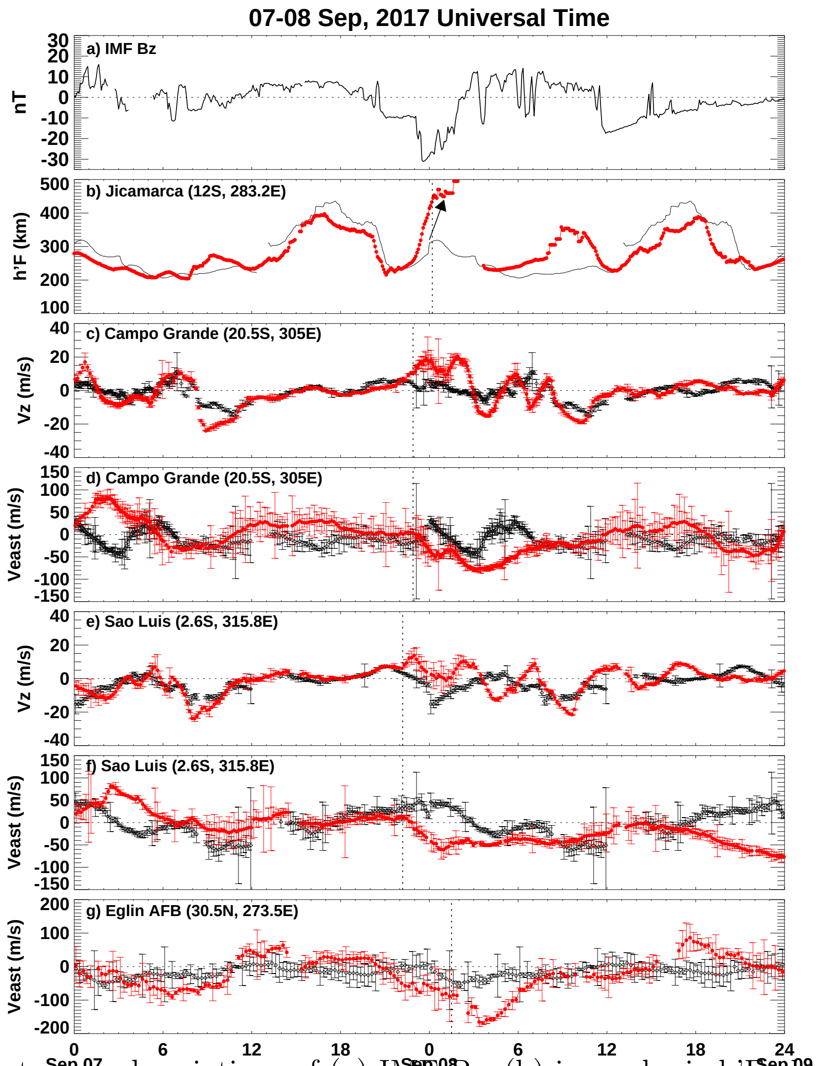

Figure 8. The temporal variations of (a) IMF B_z, (b) ionospheric h'F observed at Jicamarca, F-layer vertical drift velocity and eastward drift velocity observed at Campo Grande (c and d) and at Sao Luis (e and f), and eastward drift velocity at Eglin AFB (g) during the period of 7-8 September 2017. The black lines represent the values of geomagnetic quiet day (6 September 2017). The vertical dotted line represent the local sunset. The error bars represent the velocity spread.

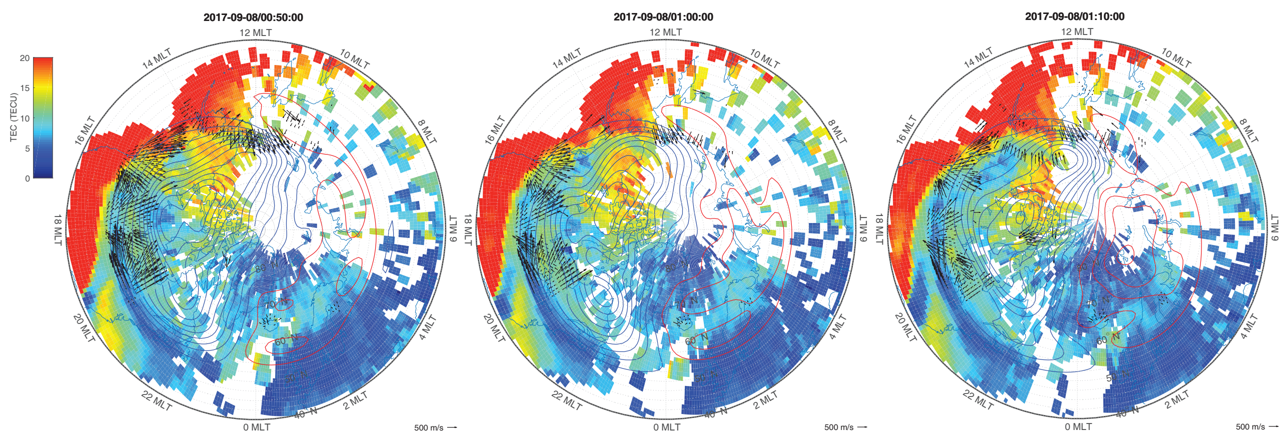

Figure 9. Polar view of the 2-D GPS vertical TEC maps over Northern Hemisphere at 0050, 0100, and 0110 UT on 8 September 2017. The blue (red) solid contours indicate negative (positive) ionospheric electrostatic potential field, which is derived from SuperDARN measurements. The black arrows represent ionospheric plasma line-of-sight velocity measurements taken by SuperDARN radars at different sites. The plot is shown in the MLT and MLAT coordinates with 12 MLT at the top.

Figure 1.

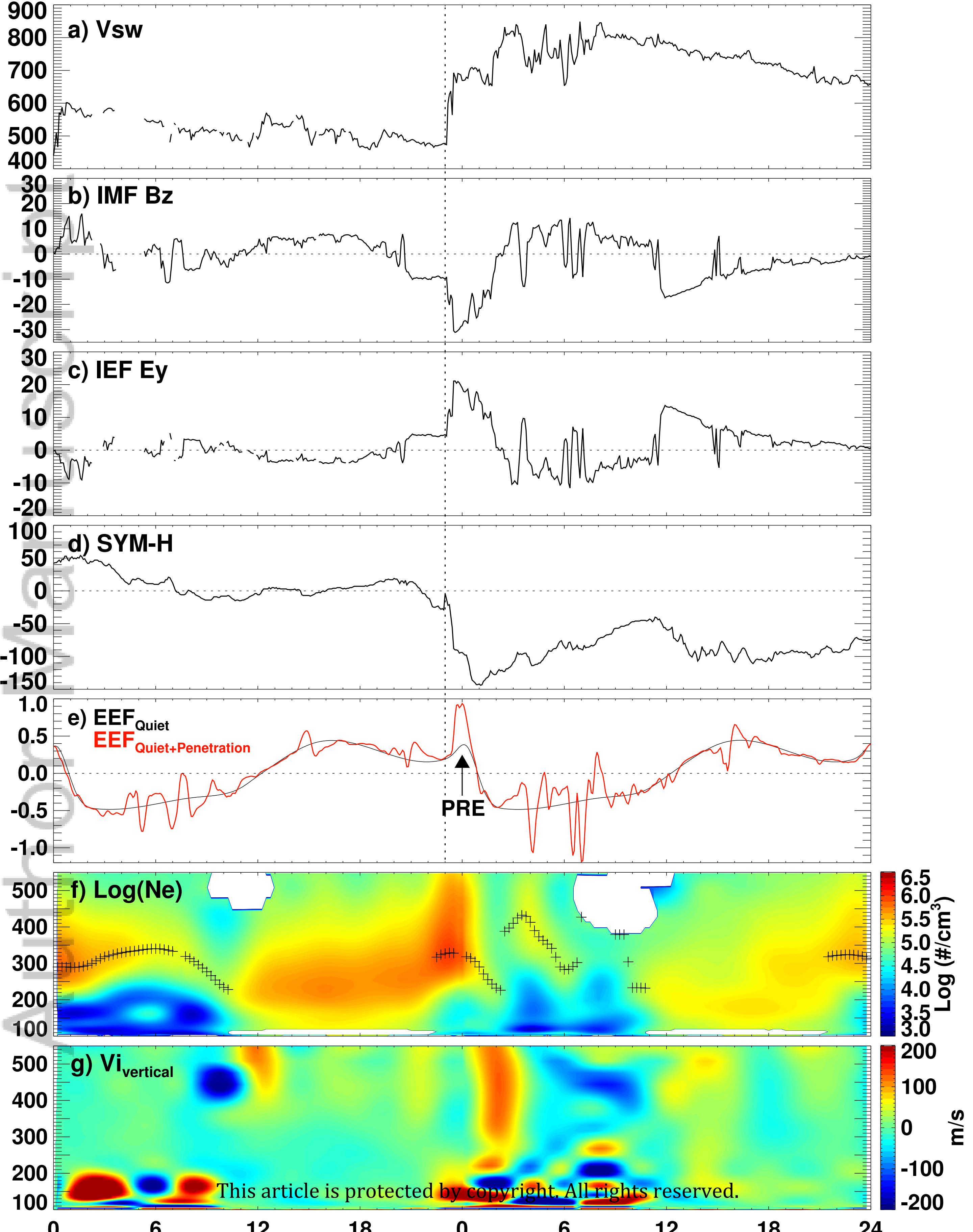
a) Vsw
b) IMF Bz
c) IEF Ey
d) SYM-H
e) EEF_Quiet
EEF_Quiet+Penetration
PRE
f) Log(Ne)
Log (#/cm3)
g) Vi_vertical
m/s
0
6
12
18
0
6
12
18
24

Figure 2.

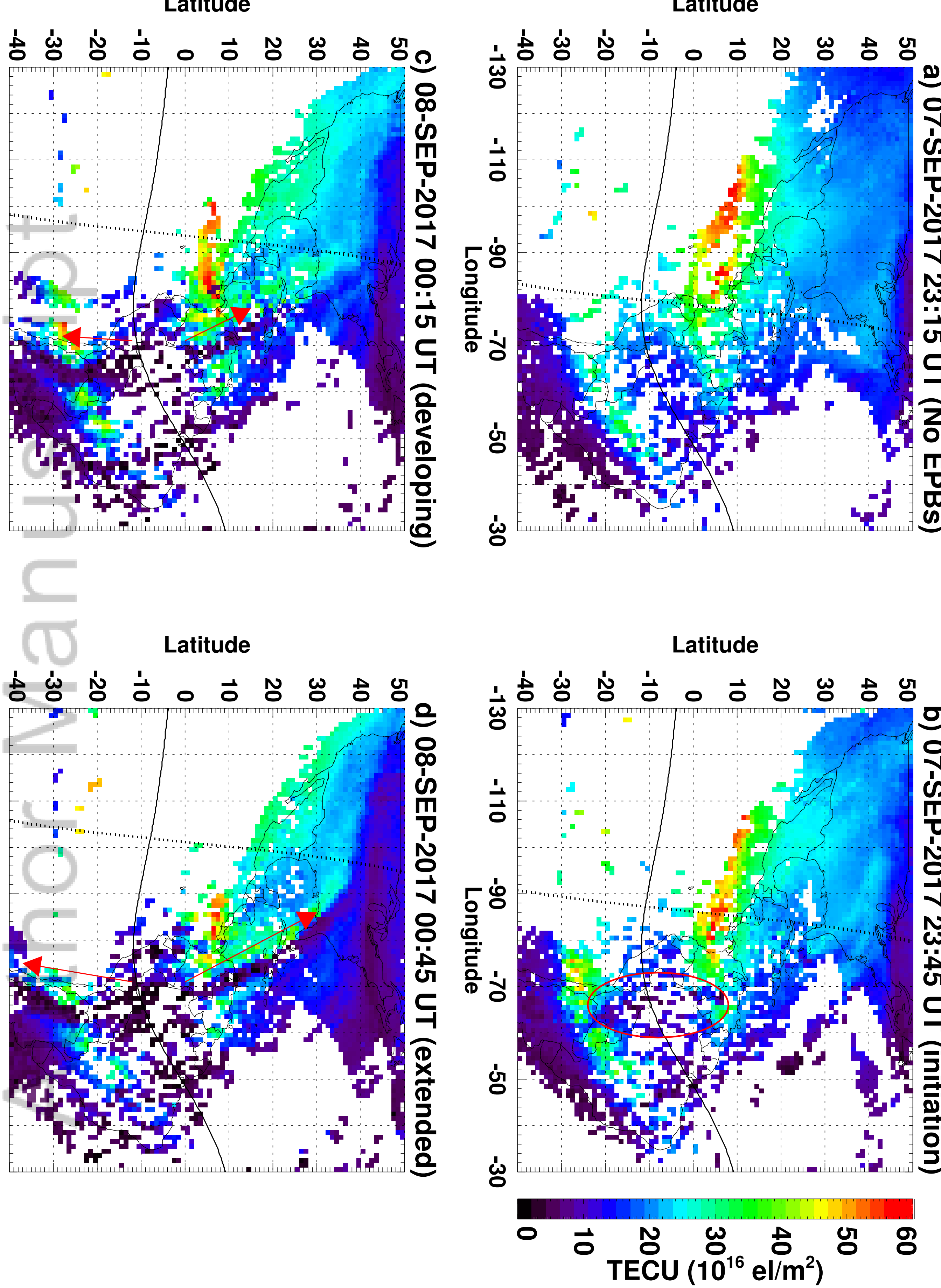
a) 07-SEP-2017 23:15 UT (No EPBs)
b) 07-SEP-2017 23:45 UT (Initiation)
c) 08-SEP-2017 00:15 UT (developing)
d) 08-SEP-2017 00:45 UT (extended)
Latitude
Longitude
TECU (10^{16} el/m^2)

Figure 3.

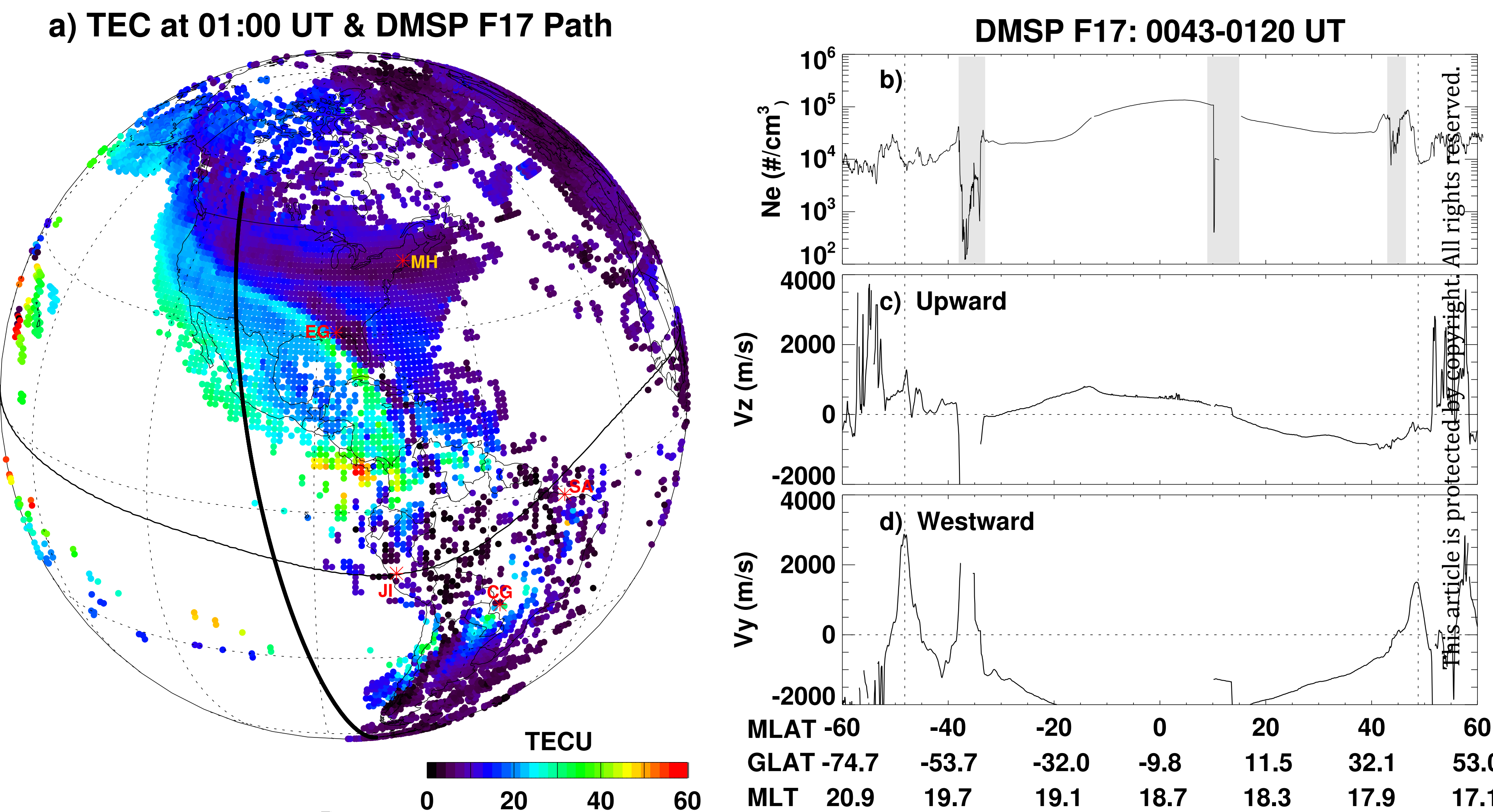

a) TEC at 01:00 UT & DMSP F17 Path
MH
EG
SA
JI
CG
TECU
0
20
40
60
DMSP F17: 0043-0120 UT
b)
Ne (#/cm^3)
10^2
10^3
10^4
10^5
10^6
c) Upward
Vz (m/s)
d) Westward
Vy (m/s)
-2000
0
2000
4000
MLAT -60 -40 -20 0 20 40 60
GLAT -74.7 -53.7 -32.0 -9.8 11.5 32.1 53.0
MLT 20.9 19.7 19.1 18.7 18.3 17.9 17.1

Figure 4.

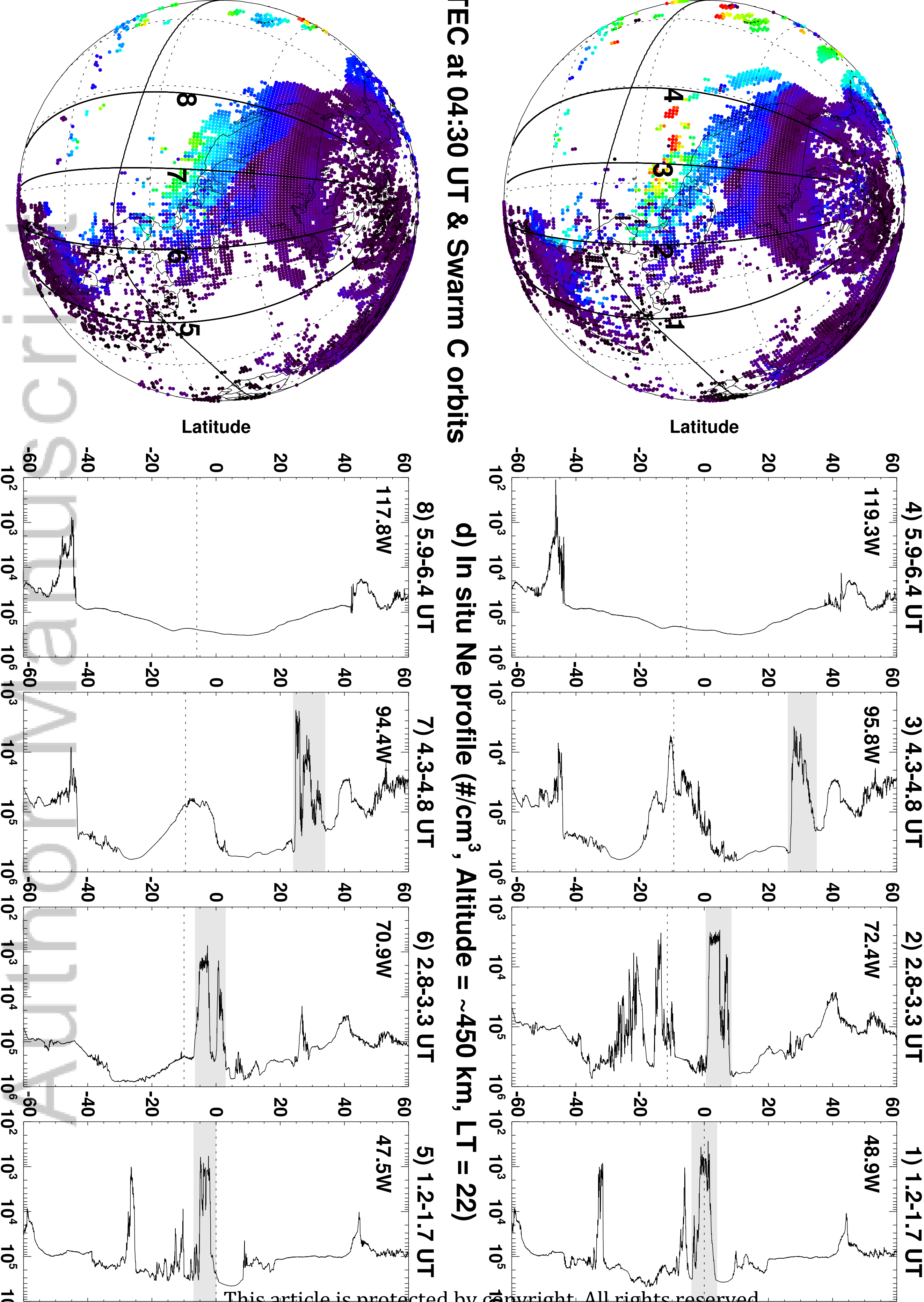

TEC at 04:30 UT & Swarm C orbits
d) In situ Ne profile (#/cm³, Altitude = ~450 km, LT = 22)
1) 1.2-1.7 UT
48.9W
2) 2.8-3.3 UT
72.4W
3) 4.3-4.8 UT
95.8W
4) 5.9-6.4 UT
119.3W
5) 1.2-1.7 UT
47.5W
6) 2.8-3.3 UT
70.9W
7) 4.3-4.8 UT
94.4W
8) 5.9-6.4 UT
117.8W
Latitude
Latitude

Figure 5.

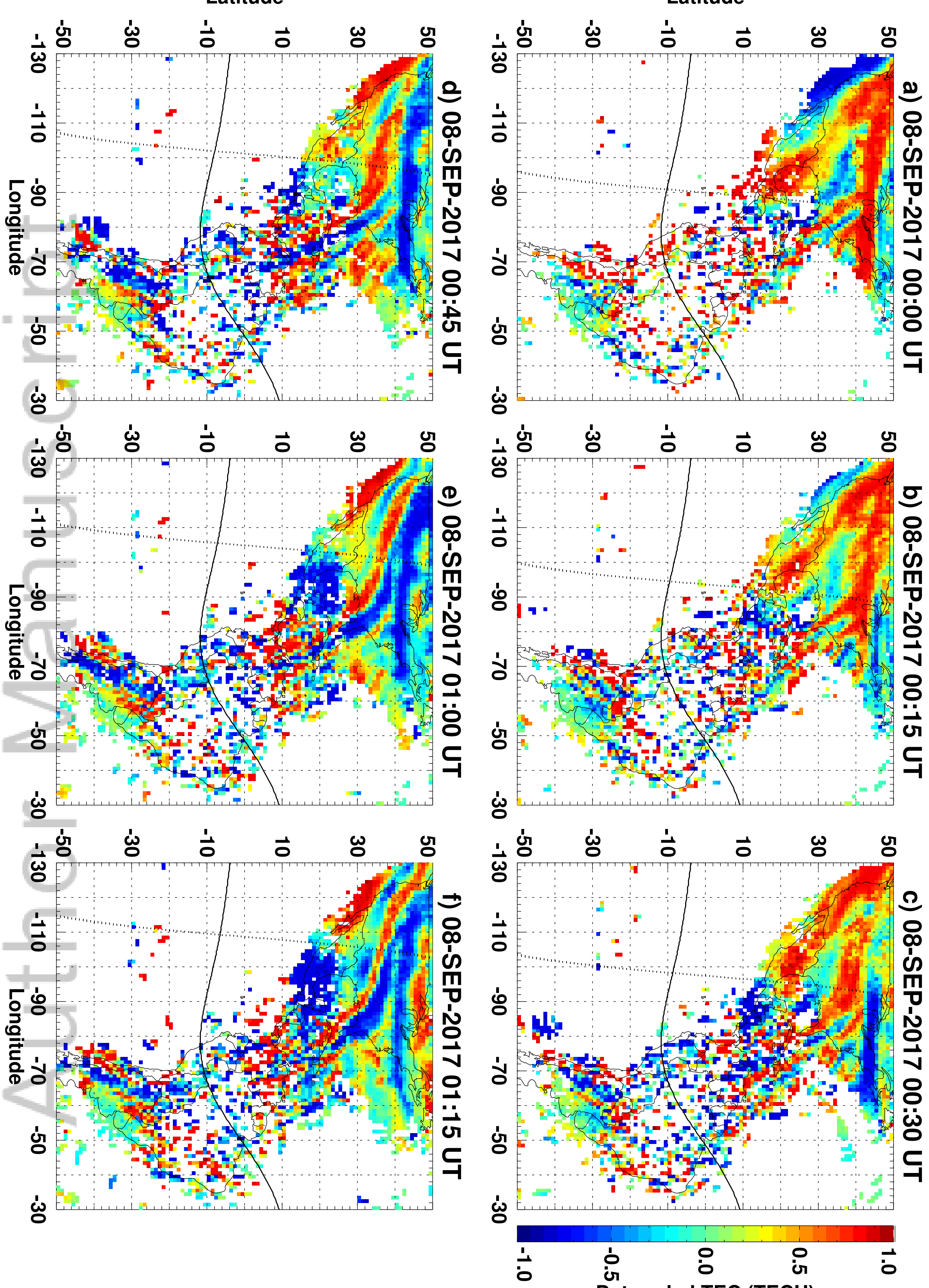
a) 08-SEP-2017 00:00 UT
b) 08-SEP-2017 00:15 UT
c) 08-SEP-2017 00:30 UT
d) 08-SEP-2017 00:45 UT
e) 08-SEP-2017 01:00 UT
f) 08-SEP-2017 01:15 UT
Latitude
Longitude
-130 -110 -90 -70 -50 -30
-50 -30 -10 10 30 50
-1.0 -0.5 0.0 0.5 1.0
Detrended TEC (TECU)

Figure 6.

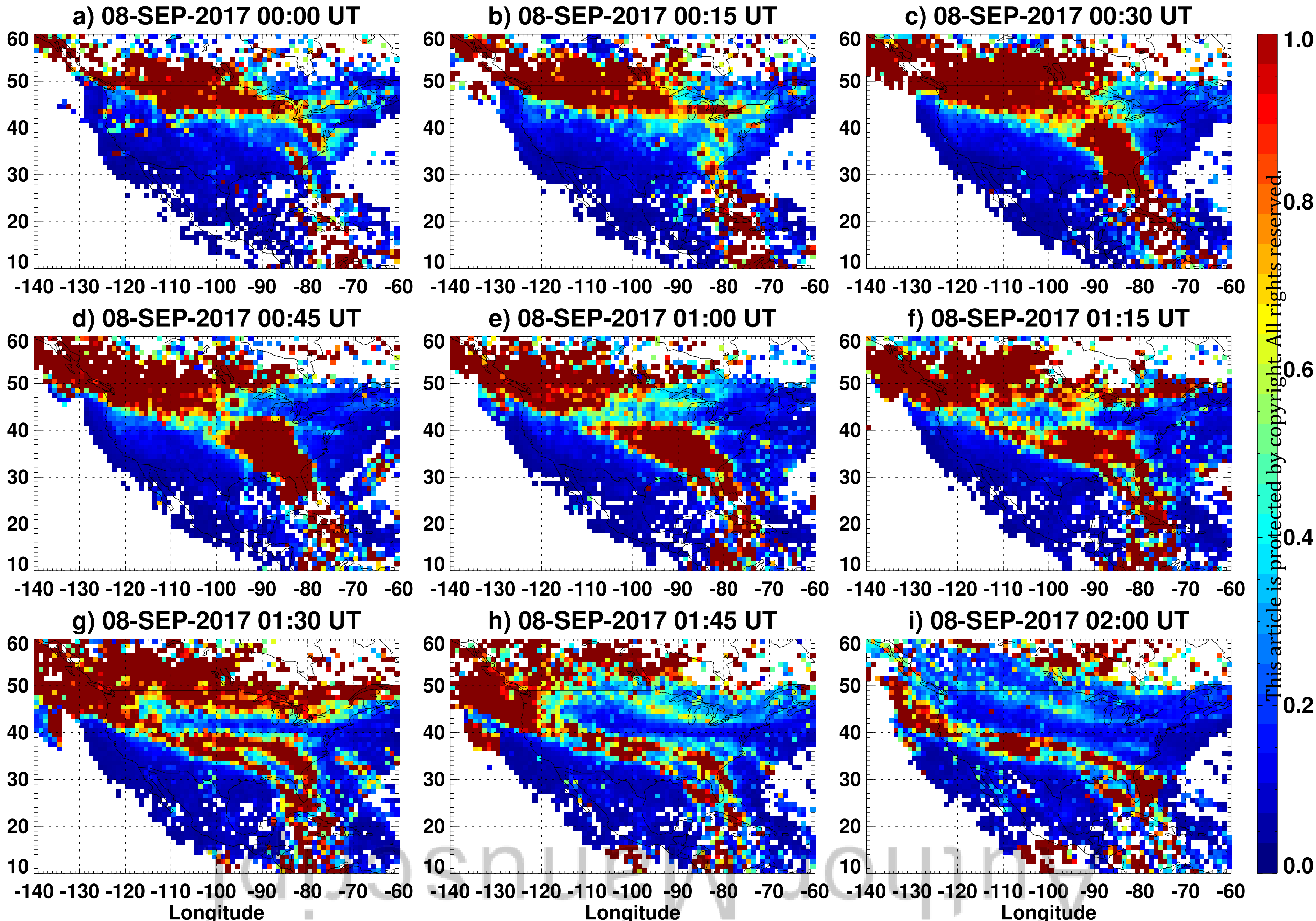

a) 08-SEP-2017 00:00 UT
b) 08-SEP-2017 00:15 UT
c) 08-SEP-2017 00:30 UT
d) 08-SEP-2017 00:45 UT
e) 08-SEP-2017 01:00 UT
f) 08-SEP-2017 01:15 UT
g) 08-SEP-2017 01:30 UT
h) 08-SEP-2017 01:45 UT
i) 08-SEP-2017 02:00 UT
Longitude
0.0
0.2
0.4
0.6
0.8
1.0

Figure 7.

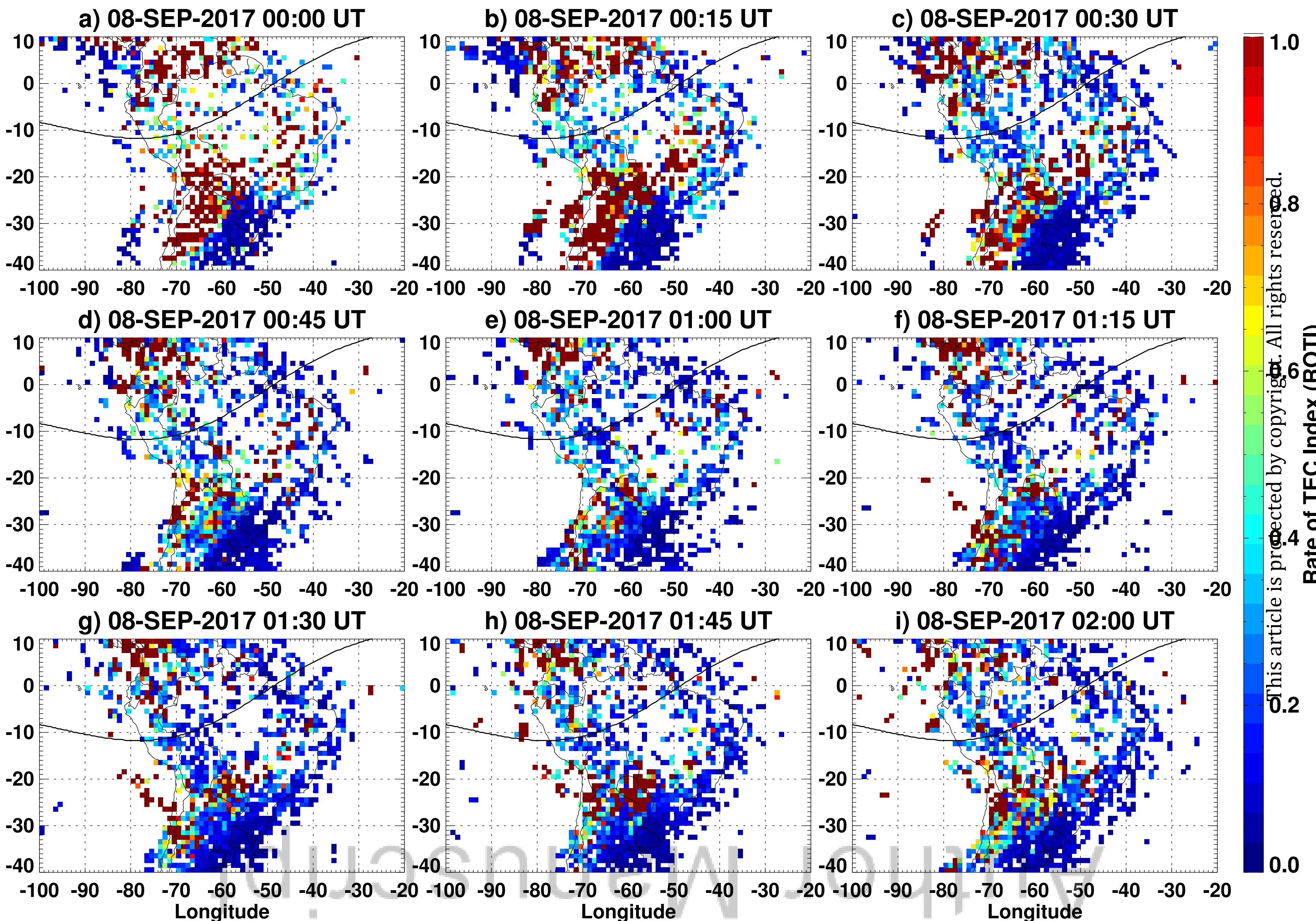

a) 08-SEP-2017 00:00 UT
b) 08-SEP-2017 00:15 UT
c) 08-SEP-2017 00:30 UT
d) 08-SEP-2017 00:45 UT
e) 08-SEP-2017 01:00 UT
f) 08-SEP-2017 01:15 UT
g) 08-SEP-2017 01:30 UT
h) 08-SEP-2017 01:45 UT
i) 08-SEP-2017 02:00 UT
Longitude
Rate of TEC Index (ROTI)

Figure 8.

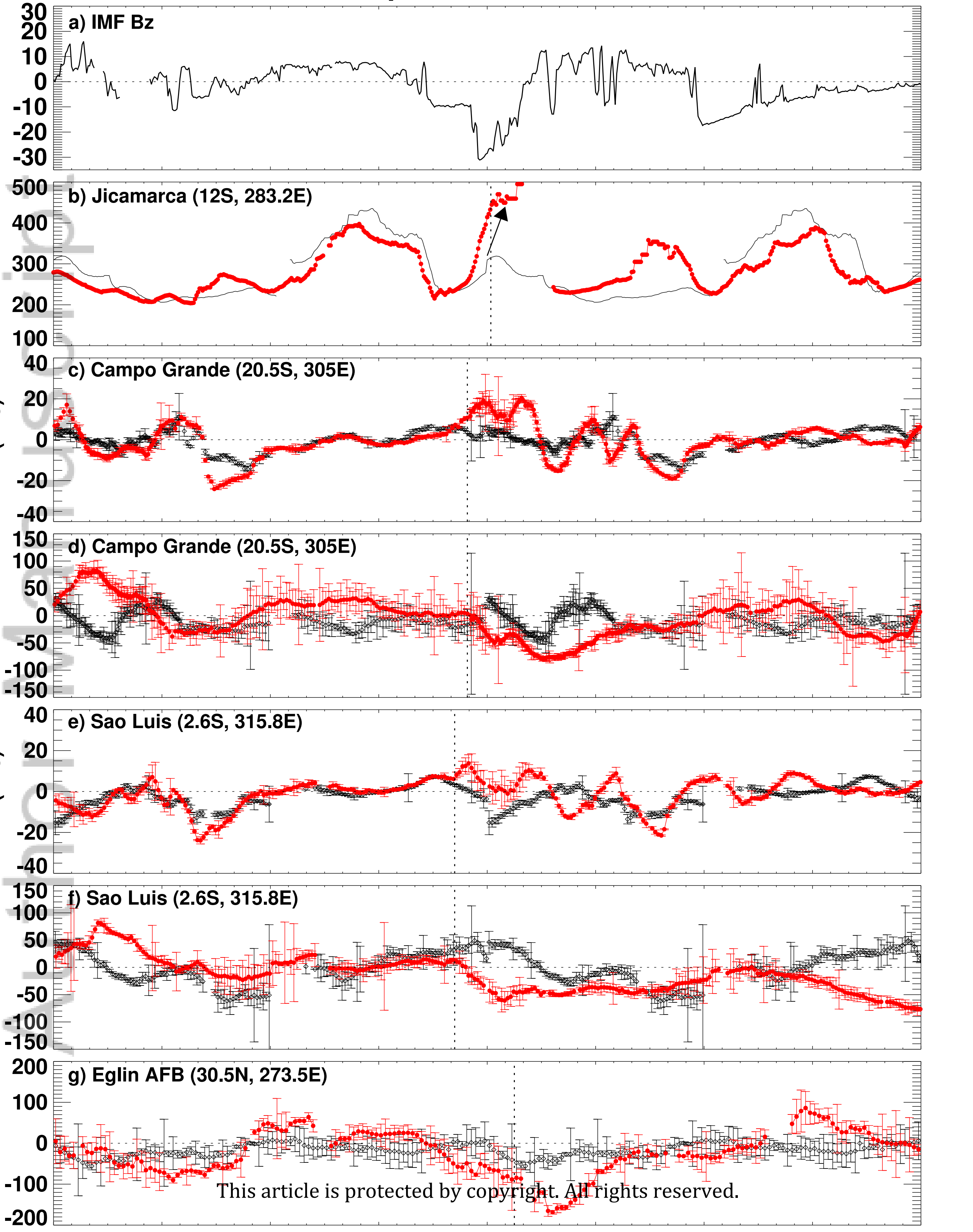

a) IMF Bz
b) Jicamarca (12S, 283.2E)
c) Campo Grande (20.5S, 305E)
d) Campo Grande (20.5S, 305E)
e) Sao Luis (2.6S, 315.8E)
f) Sao Luis (2.6S, 315.8E)
g) Eglin AFB (30.5N, 273.5E)

Figure 9.

20
15
10
5
0
TEC (TECU)
2017-09-08/00:50:00
12 MLT
14 MLT
10 MLT
16 MLT
8 MLT
18 MLT
6 MLT
20 MLT
4 MLT
22 MLT
2 MLT
0 MLT
80° N
70° N
60° N
50° N
40° N
500 m/s
2017-09-08/01:00:00
12 MLT
14 MLT
10 MLT
16 MLT
8 MLT
18 MLT
6 MLT
20 MLT
4 MLT
22 MLT
2 MLT
0 MLT
500 m/s
2017-09-08/01:10:00
12 MLT
14 MLT
10 MLT
16 MLT
8 MLT
18 MLT
6 MLT
20 MLT
4 MLT
22 MLT
2 MLT
0 MLT
500 m/s

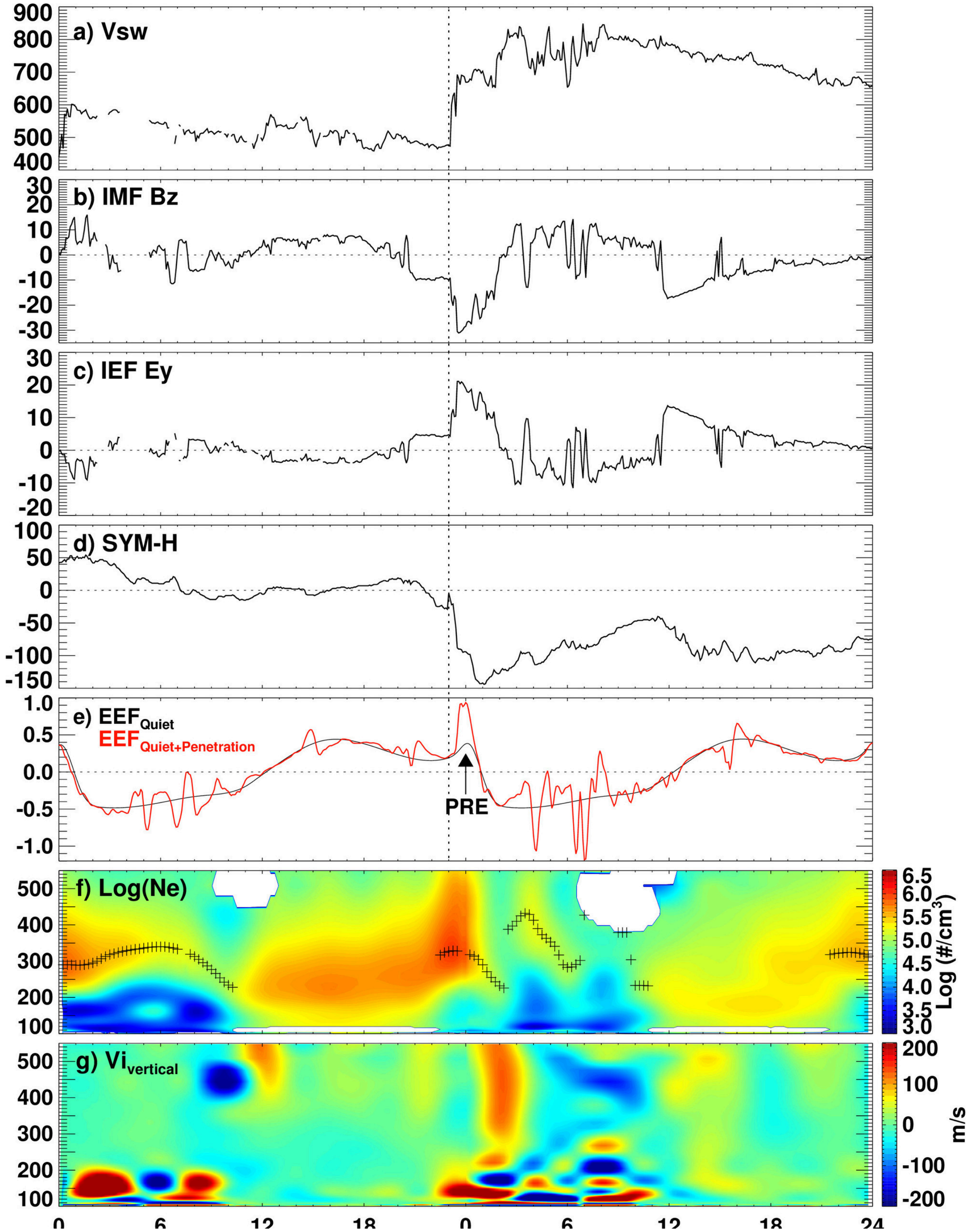

2018sw002101-f01-z-.eps

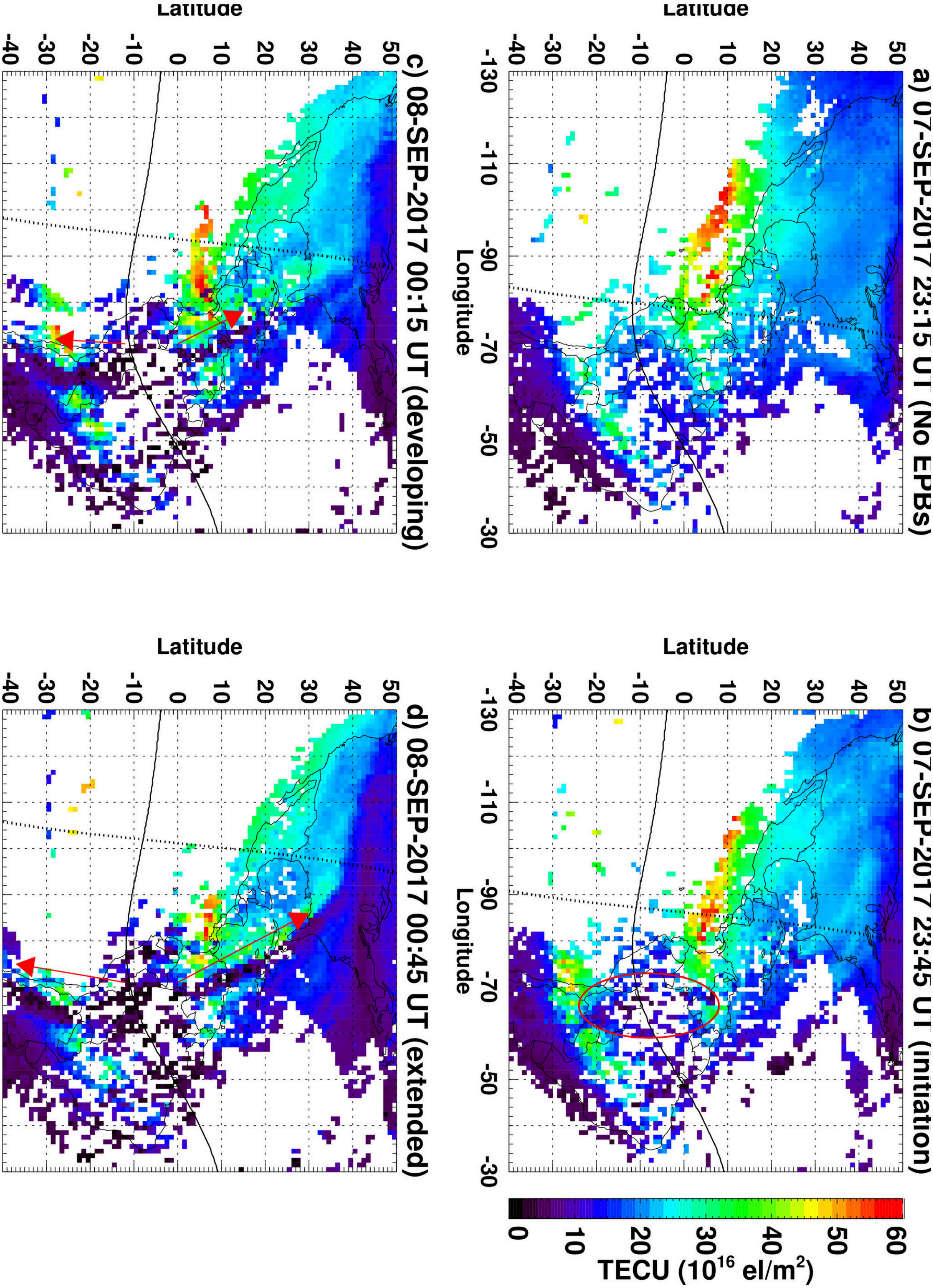

2018sw002101-f02-z-.eps

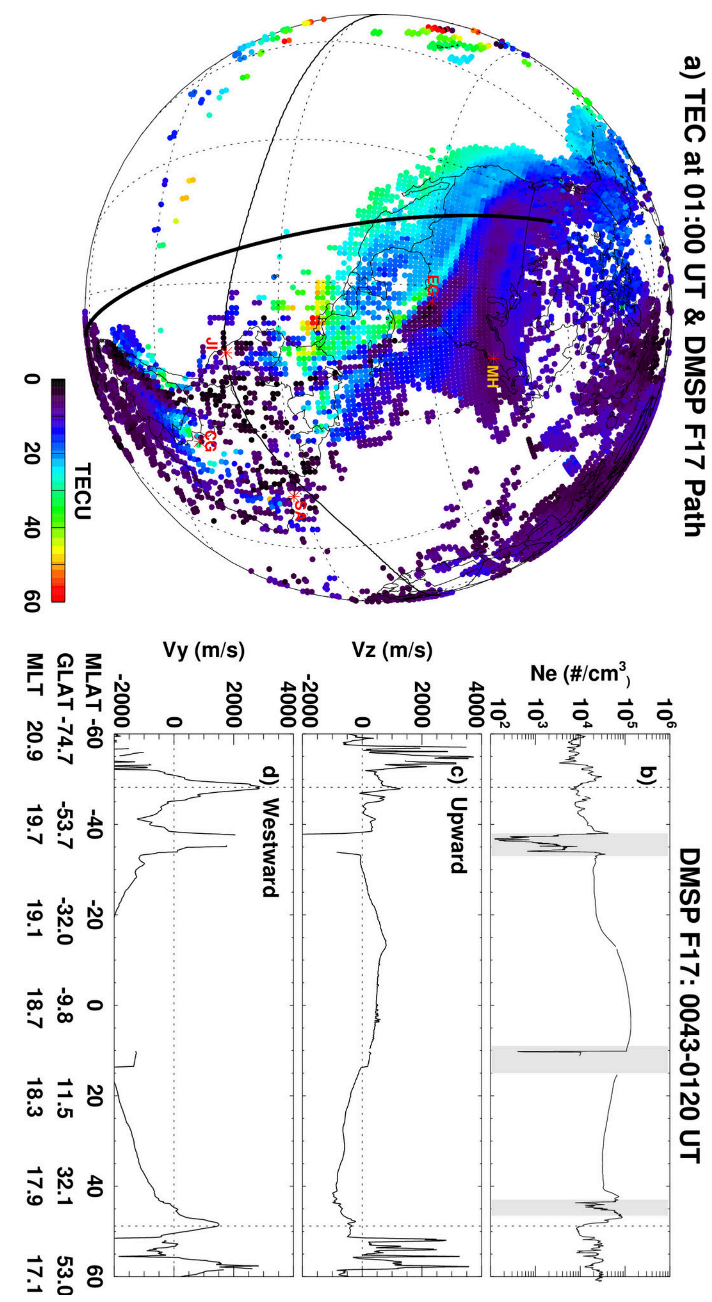

2018sw002101-f03-z-.eps

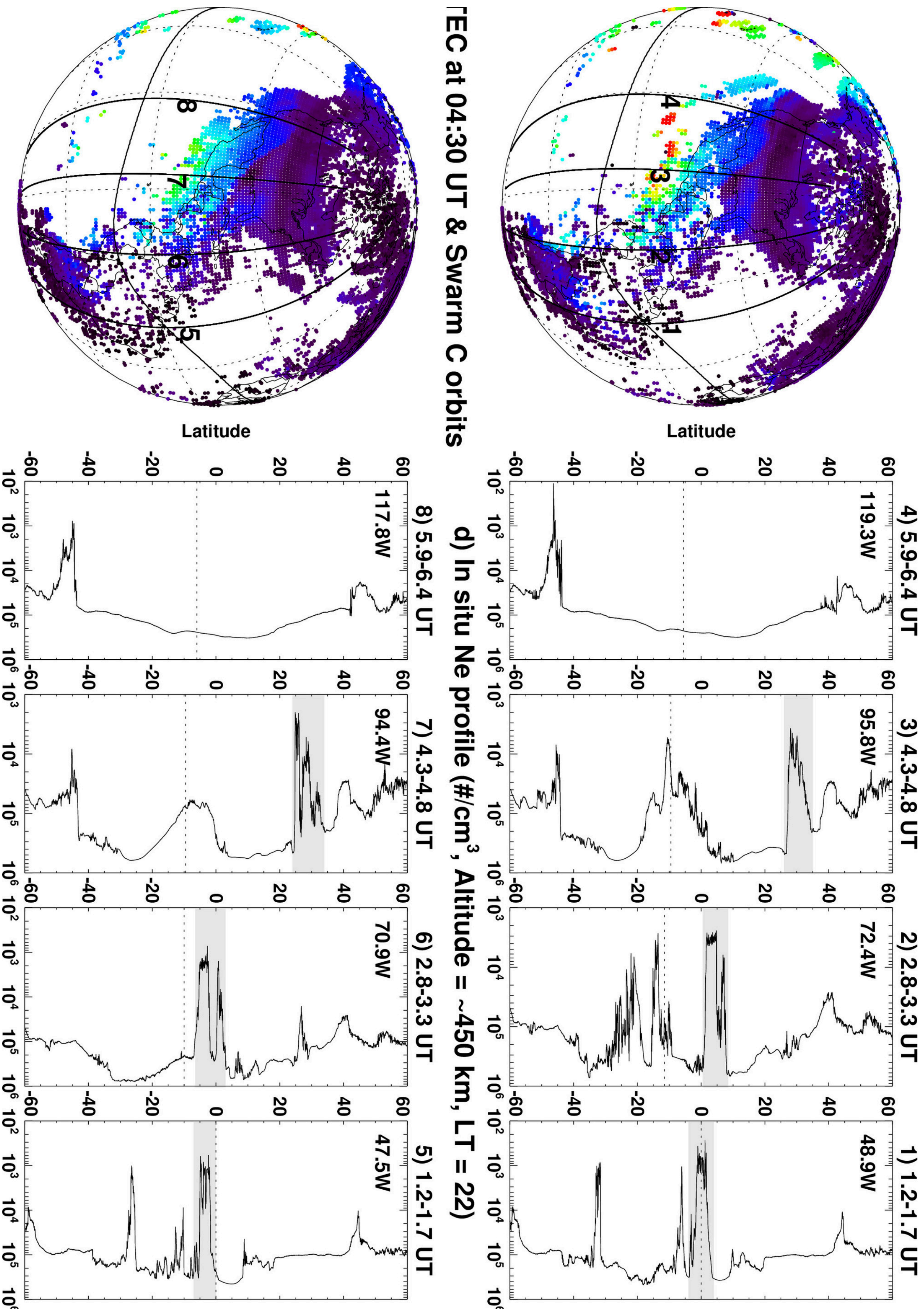

2018sw002101-f04-z-.eps

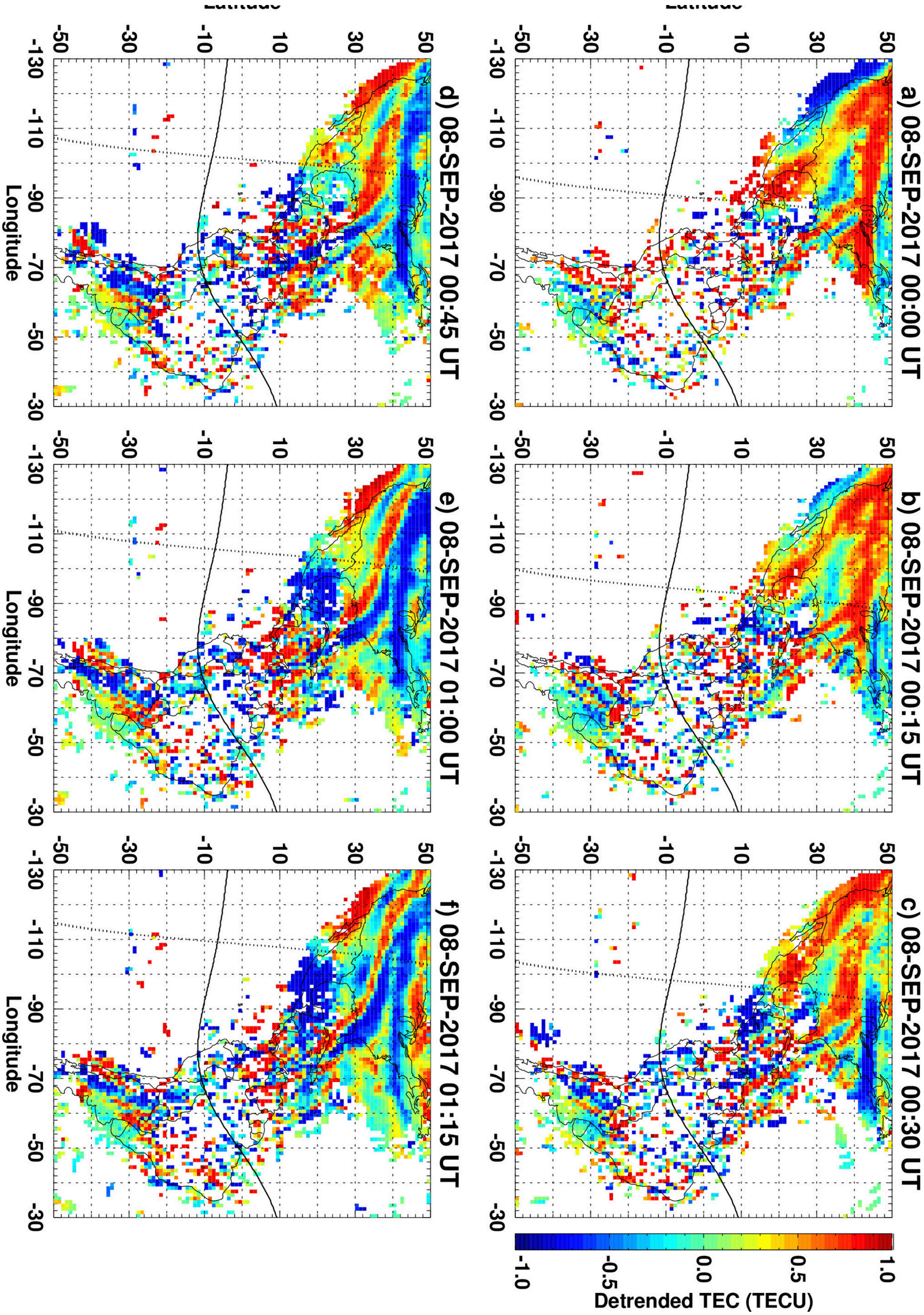

2018sw002101-f05-z-.eps

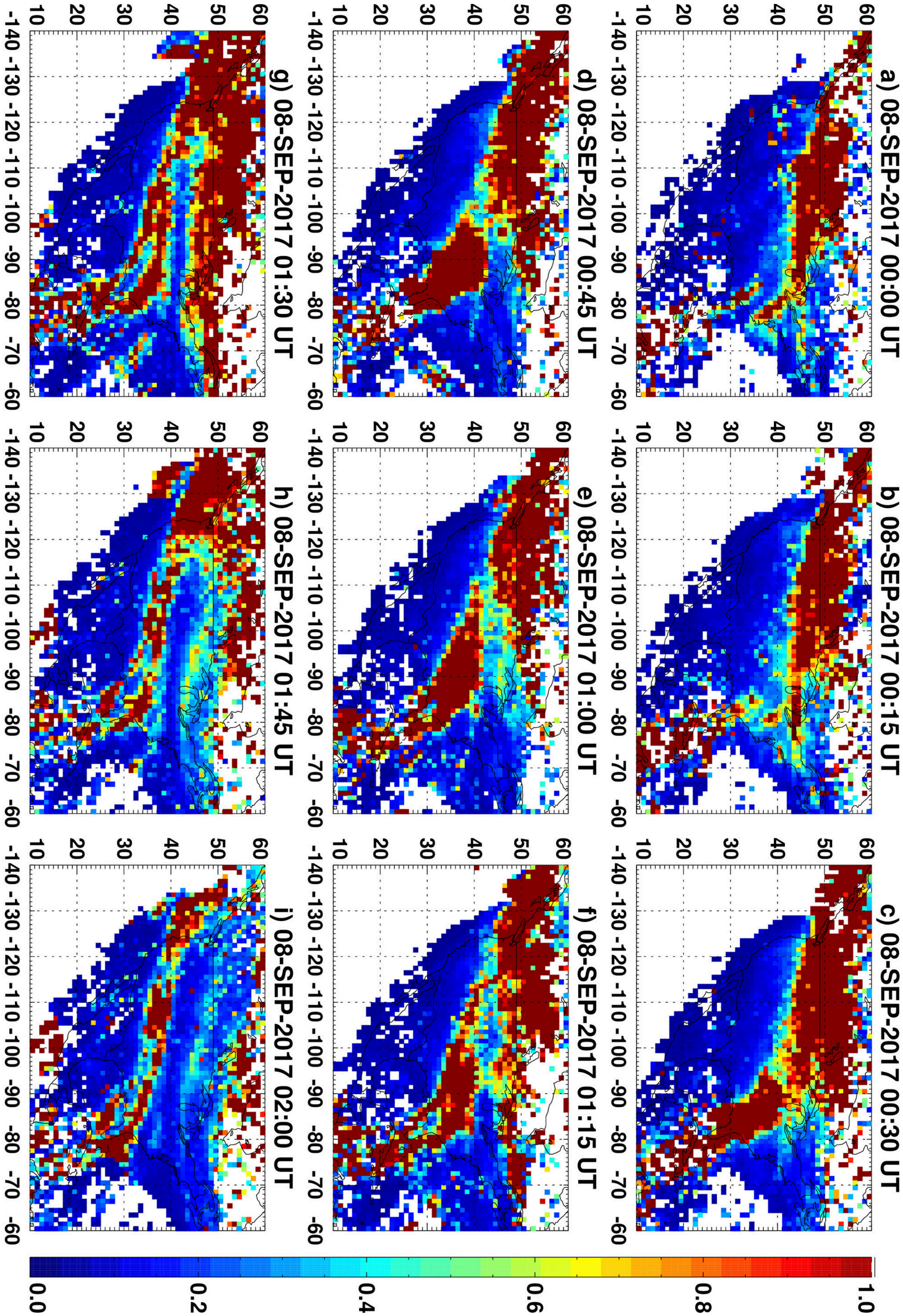

2018sw002101-f06-z-.eps

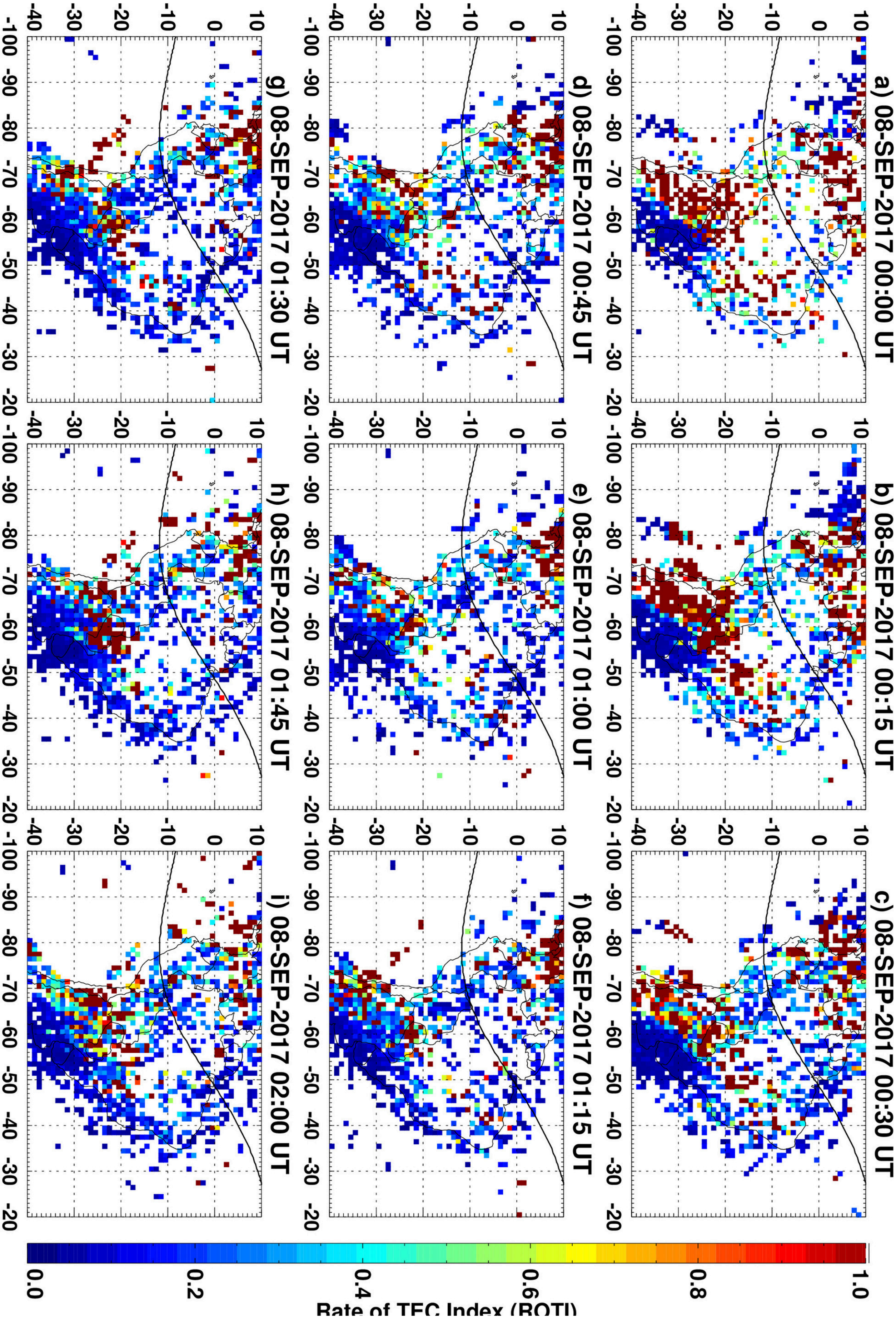

2018sw002101-f07-z-.eps

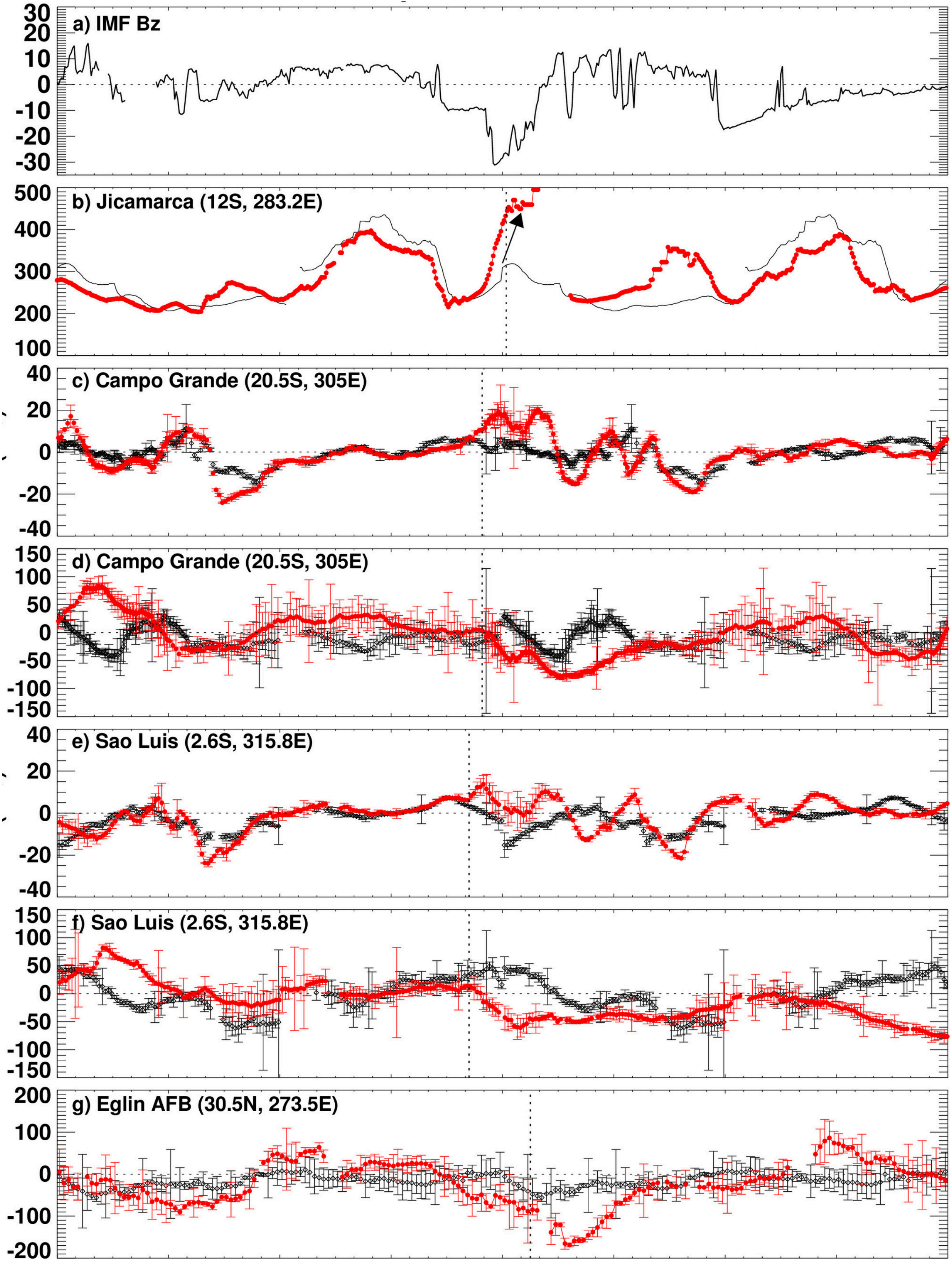

2018sw002101-f08-z-.eps

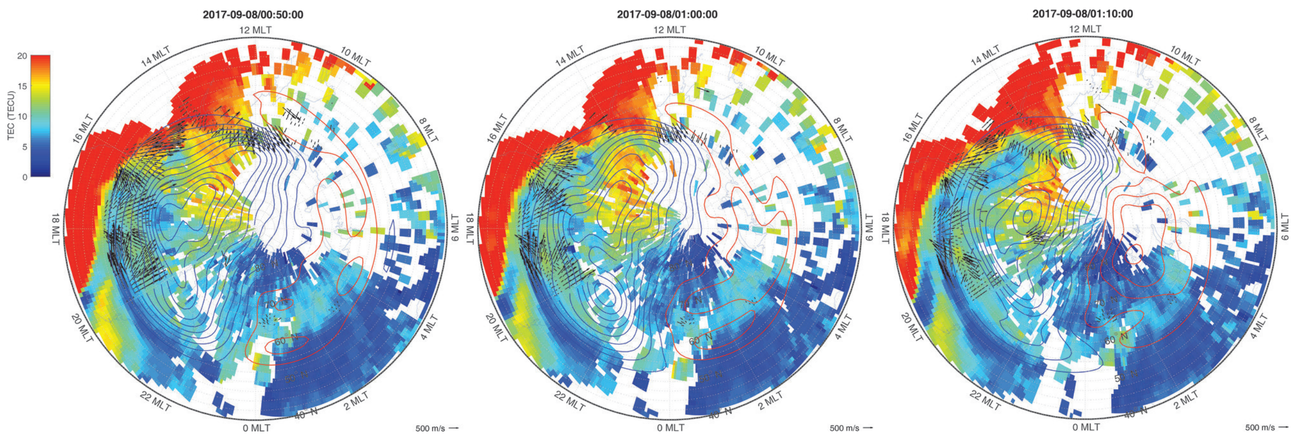

2018sw002101-f09-z-.eps